



Arab American University

Faculty of Graduate Studies

Design and Characterization of $\text{WO}_3/\text{Ga}_2\text{S}_3$ heterojunctions

By

Shatha Nazeh Abualrub

Supervisor

Prof. Atef Fayez Qasrawi

**This thesis was submitted in partial fulfillment of the
requirements for the Master's degree in Physics**

September/2019

**© Arab American University – 2019. All rights
reserved.**

Design and Characterization of $\text{WO}_3/\text{Ga}_2\text{S}_3$ heterojunctions

By

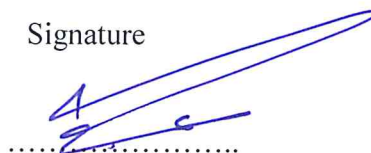
Shatha Nazeh Abualrub

This thesis was defended successfully on 28.09.2019 and approved by:

Committee members

Signature

1. Prof. Atef Fayez Qasrawi (Supervisor)



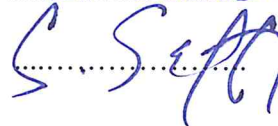
.....

2. Prof. Zaki Saleh (Internal examiner)



.....

3. Prof. Ghassan Safarini (External examiner)



.....

Declaration

The work in this thesis, unless otherwise referenced, is the researcher's own work and has not been submitted elsewhere for any other degree or qualification.

Student's Name: Shatha Nazeh Omar Abualrub.

Signature:

Date:

Dedication

To My Parents

Acknowledgment

Praise be to Allah, the Lord of the Worlds. Then, I would like to thanks the university for its president and staff. I would also like to thank the distinguished doctors, and especially the scientist Prof. Atef Qasrawi, who supervised this project and helped me to achieve it. Special thanks for Ms. Olfat Omareya who help me to finish this work. I also extend my thanks and appreciation to my dear family, especially my beloved father, my dear mother and my brothers and sisters who supported me to complete this work. I do not forget my great friends. I thank them for standing with me during this semester and throughout university life.

Abstract

In this thesis, we report the design and characterizations of $\text{WO}_3/\text{Ga}_2\text{S}_3$ heterojunction hybrid devices. The devices which are grown by the physical evaporation technique under vacuum pressure of 10^{-5} mbar are characterized by means of X-ray diffraction (XRD), scanning electron microscopy (SEM), energy dispersive X-ray spectroscopy (EDX), UV-VIS spectrophotometry, impedance spectroscopy, capacitance-voltage and current-voltage characteristics curves. While the X-ray diffraction indicated amorphous nature of the grown materials, the SEM images displayed no particular morphology confirming the amorphous nature of growth. The EDX analysis displays stoichiometric composition of the grown materials. Optically, while WO_3 and Ga_2S_3 exhibit energy band gap values of 3.17 and 2.53 eV, respectively, the $\text{WO}_3/\text{Ga}_2\text{S}_3$ interface exhibit an energy band gap of 2.62 eV and resulted in an aligned conduction band with valence band offset of 0.61 eV. The optically interfaced layers exhibit deep band tail of width of 0.78 eV. In addition, the electrical measurements has shown that the device which is coated onto Yb substrate and recoated with Au pad exhibit capacitance-voltage characteristics that nominate it for use as MOSFET devices. The current-voltage characteristics also displayed rectifying features within a barrier height of 0.73 eV under forward bias conditions. The reduction of series resistance effect indicated ideal diode characteristics. On the other hand, the impedance spectroscopy analysis had shown that the device can exhibit wide capacitance and impedance tunability in the frequency domain of 10-1800 MHz nominating it as tunable capacitors. It was also observed that the Yb/ $\text{WO}_3/\text{Ga}_2\text{S}_3/\text{Au}$ hybrid devices exhibit band stop features with notch frequency of 1.65 GHz. The test of the return loss values of the propagating ac signal displayed

high quality signal and good impedance match nominating the device for applications as band stop filters.

List of Contents

	Title	Page No.
	List of Tables	x
	List of Figures	xi
	List of Symbols	xiv
Chapter One	Introduction and literature survey	1
Chapter Two	Theoretical background	6
	2.1 The X-ray diffraction	6
	2.1.1 Bragg's law	6
	2.1.2 Scherrer equation	7
	2.1.3 Structural properties	8
	2.2 Optical Properties	9
	2.2.1 Absorption coefficient	10
	2.2.2 Tauc's Equation	11
	2.2.3 Band Tails	11
	2.2.4 The complex refractive index and dielectric constant	13
	2.2.5 Optical conductivity	13
	2.3 Electrical properties	15
	2.3.1 Current Conduction Mechanism	15
	2.3.1.1 Thermionic emission current	15
	2.4 Capacitance (C)-Voltage (V) characteristics	18
	2.5 RLC circuits	19
	2.5.1 The series RLC circuits	20
	2.5.2 The parallel RLC circuits	21
	2.4.3 The return loss	22
Chapter Three	Experimental details	23
	3.1 Cleaning glass	23
	3.2 Evaporating process and thin film preparations	23
	3.3 Thin Film analysis	25
	3.3.1 The X-ray diffraction (XRD) measurements	26

	3.3.2 Scanning Electron Microscopy (SEM) measurements	27
	3.3.3 Energy-dispersive X-ray spectroscopy (EDX)	28
	3.3.4 Optical Measurements	29
	3.3.5 The hot-probe technique	29
	3.3.6 Impedance Measurements	30
	3.3.7 The Current-Voltage Measurements	31
Chapter Four	Results and discussions	33
	4.1 Structural analysis	33
	4.2 Optical analysis	43
	4.3 Electrical properties	53
	4.3.1 Current-Voltage characteristics	53
	4.4 Energy band diagram	59
	4.5 The Capacitance (C)-Voltage (V) analysis	61
	4.6 Impedance Spectroscopy analysis	63
Chapter Five	Conclusions	68
References		70
Appendix A		77
Appendix B		81
الملخص		86

List of Tables

No.	Title	Page No.
1.1	The calculated-theoretical band offsets for $\text{WO}_3/\text{Ga}_2\text{S}_3$ heterojunctions.	4
2.2	The 3-D braves lattices for solid state materials and their conditions.	9
4.1	A structural comparison between the stacked layers of Yb/WO_3 , $\text{Yb}/\text{Ga}_2\text{S}_3$ and $\text{Yb}/\text{WO}_3/\text{Ga}_2\text{S}_3$.	38
4.2	The structural parameters of WO_3 and $\text{WO}_3/\text{Ga}_2\text{S}_3$ thin films.	38
4.3	The calculated optical measurements for WO_3 , Ga_2S_3 and $\text{WO}_3/\text{Ga}_2\text{S}_3$ thin films.	46
4.4	The values of R_s , η and ϕ_B using the derivative $dV/d(\ln(I))$ and the Cheung function $H(I)$ for $\text{Yb}/\text{WO}_3/\text{Ga}_2\text{S}_3/\text{Au}$ schottky devices.	59

List of Figures

Figure No.	Caption	Page No.
2.1	The schematic diagram of Bragg's law.	7
2.2	The transmittance, reflectance and absorbance of light that incident on an optical medium.	9
2.3	The series RLC circuit diagram.	20
2.4	The impedance triangle of series RLC circuit.	21
2.5	The parallel RLC circuit diagram.	21
3.1	The 600 VCM evaporation system.	24
3.2	The prepared thin films (a) and (b) experimentally (c) and (d) geometrical designs.	25
3.3	X-ray Rigaku diffractometer.	26
3.4	The schematic diagram of XRD.	27
3.5	The schematic diagram of SEM.	28
3.6	The UV-VIS spectrophotometer.	29
3.7	The set-up of hot-probe technique.	30
3.8	The set-up for impedance measurements using Agilent 4291B RF Signal Generator impedance analyzer.	31
4.1	The X-ray diffraction patterns for 1.0 μm WO_3 , 1.0 μm Ga_2S_3 and 2.0 μm $\text{WO}_3/\text{Ga}_2\text{S}_3$ films deposited onto glass substrates.	33
4.2	The X-ray diffraction patterns for WO_3 , Ga_2S_3 and $\text{WO}_3/\text{Ga}_2\text{S}_3$ films deposited onto Yb substrates.	35
4.3	The SEM image for $\text{WO}_3/\text{Ga}_2\text{S}_3$ heterojunction deposited on glass for (a) 1K enlargement (b) 100K enlargement (c) 300K enlargement.	40
4.4	The EDS spectra for (a) WO_3 (b) $\text{WO}_3/\text{Ga}_2\text{S}_3$ (c) Ga_2S_3 films.	42
4.5	The transmittance spectra for WO_3 , Ga_2S_3 and $\text{WO}_3/\text{Ga}_2\text{S}_3$ thin films on glass substrates.	43

4. 6	The reflectance for the WO_3 , Ga_2S_3 and $\text{WO}_3/\text{Ga}_2\text{S}_3$ thin films on glass substrates.	44
4.7	The absorption coefficient (α) for WO_3 , Ga_2S_3 and $\text{WO}_3/\text{Ga}_2\text{S}_3$ thin films.	45
4.8	The calculated indirect energy band gaps using Tauc equation fitting for WO_3 , Ga_2S_3 and $\text{WO}_3/\text{Ga}_2\text{S}_3$ thin films.	47
4.9	The determined interband energies (E_e) for WO_3 , Ga_2S_3 and $\text{WO}_3/\text{Ga}_2\text{S}_3$ thin films.	48
4.10	The real part of dielectric constant for WO_3 , Ga_2S_3 and $\text{WO}_3/\text{Ga}_2\text{S}_3$ thin films.	49
4.11	The imaginary part of dielectric constant for WO_3 , Ga_2S_3 and $\text{WO}_3/\text{Ga}_2\text{S}_3$ thin films.	51
4.12	The optical conductivity spectra for WO_3 , Ga_2S_3 and $\text{WO}_3/\text{Ga}_2\text{S}_3$ thin films.	52
4.13	The current-voltage characteristic for $\text{Yb}/\text{WO}_3/\text{Ga}_2\text{S}_3/\text{Au}$ device.	54
4.14	The $\ln(I)$ -V characteristic for $\text{Yb}/\text{WO}_3/\text{Ga}_2\text{S}_3/\text{Au}$ device.	55
4.15	The $\ln(I)$ -V plot at (a) forward and (b) reverse bias for $\text{Yb}/\text{WO}_3/\text{Ga}_2\text{S}_3/\text{Au}$ device.	56
4.16	Plot of $dV/d(\ln I)$ versus I at (a) forward (b) reverse bias for $\text{Yb}/\text{WO}_3/\text{Ga}_2\text{S}_3/\text{Au}$ device.	57
4.17	Plot of $H(I)$ versus I at (a) forward and (b) reverse directions for $\text{Yb}/\text{WO}_3/\text{Ga}_2\text{S}_3/\text{Au}$ device.	58
4.18	The energy band diagram for $\text{Yb}/\text{WO}_3/\text{Ga}_2\text{S}_3/\text{Au}$ device.	61
4.19	The capacitance-Voltage characteristic, inset-1 shows the $C^2 - V$ variations for $\text{Yb}/\text{WO}_3/\text{Ga}_2\text{S}_3/\text{Au}$ device.	62
4.20	The capacitance for $\text{Yb}/\text{WO}_3/\text{Au}$ and $\text{Yb}/\text{WO}_3/\text{Ga}_2\text{S}_3/\text{Au}$ devices.	63
4.21	The impedance for $\text{Yb}/\text{WO}_3/\text{Au}$ and $\text{Yb}/\text{WO}_3/\text{Ga}_2\text{S}_3/\text{Au}$ devices.	64

4.22	The conductance for Yb/WO ₃ /Au and Yb/WO ₃ /Ga ₂ S ₃ /Au devices.	65
4.23	The reflection coefficient(ρ) for Yb/WO ₃ /Au and Yb/WO ₃ /Ga ₂ S ₃ /Au devices.	66
4.24	The return loss (L_r) for Yb/WO ₃ /Au and Yb/WO ₃ /Ga ₂ S ₃ /Au devices.	67

List of Symbols

Symbol	Acronym
WO_3	Tungsten Oxide
Ga_2S_3	Gallium Sulfide
λ	Wavelength
θ	Bragg angle
d	Interplanner distance
N	Integer
β	Full width at half maximum (FWHM)
D	Grain size
a	The lattice constant in the a-axis
ε	Strain
δ	Dislocation density
SF%	Stacking faults
α	Absorption coefficient
E_g	Energy band gap
\hbar	Planck's constant
ω	The angular frequency of photon
H'	The perturbation Hamiltonian
\vec{A}	Vector potential
\vec{p}	The momentum of electron
m_0	Mass of free electron
$g(E)$	The density of states
m^*	The mass effective
k	Wave vector
K	Extinction coefficient
$\tilde{N}_{\text{complex}}$	The complex refractive index
σ	Optical conductivity
ε_{eff}	The effective dielectric constant
ε_r	The real part of the dielectric constant
ε_{im}	The imaginary part of the dielectric constant
ψ_{bi}	The built in voltage
ϕ_B	The barrier height
H	The ideality factor
Q_{sc}	The space charge per unit area
ρ	The charge density
ε_s	The semiconductor dielectric constant.
W_D	The depletion width
Z	Impedance
L	Inductance
C	Capacitance
L_r	The return loss

Chapter One

Introduction and Literature Survey

Heterojunction devices including Tungsten Oxide and Gallium Sulfide play important roles in various applications. Tungsten oxide is frequently used to manufacture tungstates for x-ray screen phosphors and in gas sensors [1]. Also, it is reported that it has been investigated to be used in electrochromic, solar energy, gasochromis and optical devices [2]. Moreover, WO_3/TiO_2 composite nanotubes are employed as photocatalysis, solar cells and chemical sensors were reported [3]. In another work, $\text{Cu}/\text{WO}_3/\text{Pt}$ structure is demonstrated for nonvolatile memory applications as an RRAM [4]. In another work, It is mentioned that $\text{WO}_3/\text{BiVO}_4$ heterojunction enhances the photoconversion efficiency and increases the photocorrosion stability [5].

On the other hand, Ga_2S_3 has novel characteristics that reflect its function in technological applications. It is reported that this compound is used for terahertz applications [6]. In addition, the $\text{GaAs}/\text{Ga}_2\text{S}_3$ interfaces are mentioned to be suitable for high-power laser radiation [7]. The dielectric modeling and analysis on the $\text{Ge}/\text{Ga}_2\text{S}_3$ interface indicates the possibility of low/high band pass filter properties in the range of Plasmon frequency of 1.3-2.3 GHz [8]. In another recent study, $\text{Au}/\text{Ga}_2\text{S}_3/\text{Yb}$ is investigated to be used as tunable varactor diodes which are designed for high frequency applications such as radiowave resonators [9].

There are different techniques to prepare thin films. As an example, electron beam evaporation technique which is used to demonstrate the electrochromic and photocatalytic properties of Vanadium-doped tungsten trioxide thin films [10]. Another

method, is the hot-wire chemical-vapor deposition (HWCVD) process that motivated the growth of crystalline WO_3 nanoparticles [2]. The RF magnetron sputtering method is employed to prepare WO_3 thin films in different conditions [11] and thin films of LiS_2 , GeS_2 and Ga_2S_3 glass system were prepared by sputtering technique [12]. Moreover, the synthesizing of nanolayered $\gamma\text{-Ga}_2\text{S}_3$ into the 2D materials family can be done via the space-confined chemical vapor deposition technique [13]. Molecular beam epitaxy of WO_3 on sapphire substrates is also mentioned [14]. Furthermore, pulsed laser deposition technique is used to prepare $\text{Ga}_2\text{S}_3\text{-GeS}_2$ thin films [15]. Another mentioned work, WO_3 and MoO_3 thin films were prepared by the thermal vacuum evaporation method and their characteristics were studied [16]. Particularly, the most common preparation technique which will be used in our study is the physical vapor deposition while two films are deposited onto each other under vacuum pressure of 10^{-5} mbar. Such as, the preparation of $\text{Au/In}_4\text{Se}_3/\text{Ga}_2\text{S}_3/\text{C}$ interfaces which were prepared by physical vapor deposition technique with the exact needed thicknesses [17].

The structure of every material differs from the others, solid state material can be crystal (single crystal or polycrystalline) or amorphous. For our materials WO_3 and Ga_2S_3 , both exhibit the polymorphic structures. WO_3 has five-different structures, the cubic structure with lattice constant of $a = 3.82 \text{ \AA}$ [18]. The monoclinic structure with lattice parameters of $a = 7.306 \text{ \AA}$, $b = 7.540 \text{ \AA}$, $c = 7.692 \text{ \AA}$, $\beta = 90.881^\circ$ [19]. Triclinic structure where their parameters are $a = 7.309 \text{ \AA}$, $b = 7.522 \text{ \AA}$, $c = 7.678 \text{ \AA}$, $\alpha = 88.81^\circ$, $\beta = 90.92^\circ$, $\gamma = 90.93^\circ$ [19]. While the orthorhombic structure has $a = 7.384 \text{ \AA}$, $b = 7.512 \text{ \AA}$, $c = 3.846 \text{ \AA}$ [20], the tetragonal structure (high temperature phase) exhibit lattice parameters of $a = 5.36 \text{ \AA}$, $c = 3.98 \text{ \AA}$ [21]. Similar polymorphic structure is observed for Ga_2S_3 , three

polyphases were possibly formed, monoclinic phase (α -Ga₂S₃) wurtzite type with lattice parameters are $a = 11.094 \text{ \AA}$, $b = 9.578 \text{ \AA}$, $c = 6.395 \text{ \AA}$, $\beta = 141.15^\circ$ at $T = 1020 \text{ K}$, the second is hexagonal phase (β -Ga₂S₃) wurtzite type which have $a = 3.678 \text{ \AA}$, $c = 6.016 \text{ \AA}$ at $T = 820 \text{ K}$, the third one is cubic (γ -Ga₂S₃) zincblend type with lattice constant $a = 5.17 \text{ \AA}$ at $T = 873 \text{ K}$ [22]. Both materials include defects. For Ga₂S₃ the concentration of native defects is about 10^{22} cm^{-3} [23]. α -Ga₂S₃ has an ordered vacancies while β -Ga₂S₃ and γ -Ga₂S₃ have disordered vacancies [22]. The bond length of Ga-S is 2.32 \AA which makes it less probable to replace the sulfur atom with any one that has larger bond length with Ga atom [24]. An important structural property is strain which is inversely proportional to the grain size and it is a bond length dependent. For example, the strain of Se/Ga₂S₃ was evaluated as 11.22×10^{-3} [25]. Whereas, the defects in WO₃ are surface oxygen vacancies, after annealing ordered vacancies are produced [26]. For WO₃ it was observed that the square of the tetragonal-tetragonal strain is inversely proportional to the temperature [27].

On the other hand, the electrical properties for both materials are different, the electrical conductivity is temperature dependent and equals $10^{-14} (\Omega \cdot \text{cm})^{-1}$ for Ga₂S₃ [22]. It was reported that the electrical conductivity of InSe/Ga₂S₃ decreases with decreasing temperature, so the dark and illuminated activation energies in the temperature range of 330-250 K are 88 and 52 meV, whereas in the range of 240-160 K are 24 and 14 meV, respectively [28]. In the case of WO₃, the variation of electrical conductivity with temperature indicates semiconducting behavior [29]. Moreover, the activation energy of WO₃ was measured to be 1.04 eV [30].

The optical properties are important characteristics which are responsible of various features of the solid materials. The energy band gap exhibited values of 3.44 eV and 2.48 eV for monoclinic and hexagonal Ga_2S_3 , respectively [22]. WO_3 can be characterized as a semiconductor with an indirect band gap of 3.25 eV [30, 31]. Moreover, the electron affinities are reported to be 3.30 eV [32] and 3.33 eV [33] for Ga_2S_3 and WO_3 , respectively. Using these information the band offsets were determined and tabulated on Table 1.1.

Table 1.1: The calculated-theoretical band offsets for $\text{WO}_3/\text{Ga}_2\text{S}_3$ heterojunctions.

Interfaces	$\Delta E_g(\text{eV})$	$\Delta E_c(\text{eV})$	$\Delta E_v(\text{eV})$
$\text{WO}_3/\text{Ga}_2\text{S}_3$ (monoclinic Ga_2S_3)	0.19	0.03	0.16
$\text{WO}_3/\text{Ga}_2\text{S}_3$ (hexagonal Ga_2S_3)	0.77	0.03	0.74

For the process of quantum confinement, it is necessary to have a valence band offset larger than 0.5 eV. This value is minimum effective discontinuity for the production of thin film transistors.

In this thesis, the preparation and the formation of $\text{WO}_3/\text{Ga}_2\text{S}_3$ heterojunctions will be discussed. Namely, the structural properties will be studied by means of X-ray Rigaku diffractometer, SEM and EDX where the optical properties and dielectric will be measured via UV-VIS spectrophotometer. In addition, the impedance measurements and electrical characteristics and the energy band gap formation will be investigated. In the second chapter, the important theoretical investigations that are needed to determine the physical constants are reported and some of the important derivations are also shown. In the third chapter, the experimental details that were carried out during preparation and characterization are reported. In the fourth chapter, we report the important

measurements and the related interpretations of the results. In the last chapter, the conclusion remarks are mentioned.

Chapter Two

Theoretical Background

2.1 The X-ray diffraction

The amorphous and crystalline nature of solid state materials can be detected by X-ray diffraction; in this method the XRD patterns are obviously observed. The theoretical background that helps us to find the interplaner distance between two planes of atoms is Bragg's Law. Determining the interplaner distance, the lattice constants and then the structure of the crystalline material can also be calculated.

2.1.1 Bragg's law

Consider two planes of atoms and a monochromatic X-ray beam incident on the planes at some angle θ to the plane surface, if the path difference between two waves is n times the wavelength then a constructive interference occurs.

The following equation represents Bragg's law under constructive interference condition [34]:

$$2d \sin \theta = n\lambda \quad (2.1)$$

Where d is the interplaner distance between two plans of atoms which is of order of few angstrom, θ is the incident angle between the incident beam and the plane surface, $n = 1, 2, 3, \dots$ represents the order of reflection maximum, λ is the wavelength of the incident X-ray wave which is equals to 1.5405 Å. Fig. 2.1 displays a schematic diagram of Bragg's law.

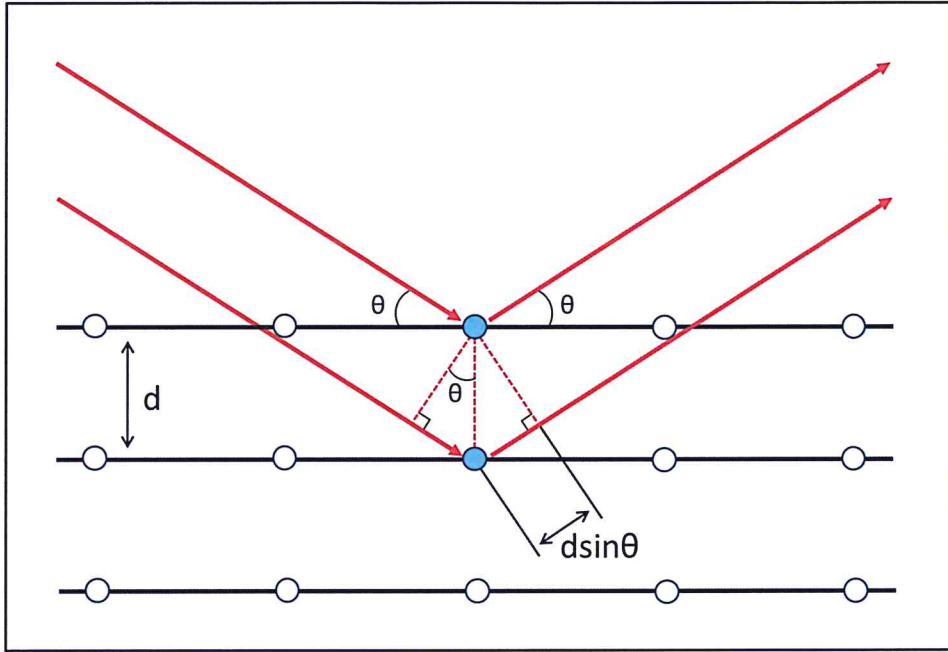


Fig. 2.1: The schematic diagram of Bragg's law.

2.1.2 Scherrer equation

The simplest way to obtain the Scherrer equation is to take the derivative of Bragg's law holding the wavelength constant and allowing the Bragg spacing and the diffraction angle to vary,

Take derivative of Eqn.(2.1) in d and θ yields

$$2\Delta d \cos\theta \Delta\theta = \lambda$$

Since $\Delta\theta$ can be positive or negative the absolute value must be taken and it reflects the half-width of the peak so $2\Delta\theta$ is the peak of full-width at half-maximum (β). Δd reflects the crystallite thickness

$$\text{Thickness} = t = \Delta d = \frac{\lambda}{\beta \cos\theta} \quad (2.2)$$

If a Gaussian function (rather than a triangle function) is used to describe the peak a prefactor of 0.94 occurs so the Scherrer equation is given by

$$t = \frac{0.94\lambda}{\beta \cos\theta} \quad (2.3)$$

Where β is the full-width at half maximum.

$$\text{So, } D = \frac{0.94\lambda}{\beta \cos\theta} \quad (2.4)$$

2.1.3 Structural properties

The study of XRD patterns is vital to determine the structural properties including grain size (D), strain (ϵ), dislocation density (δ) and stacking faults (SF). These parameters are calculated from the broadening width β (FWHM) of the most intensive peak by using the following relations [35]:

Grain size (D): is the diameter of individual grain in the crystal [36].

$$D = \frac{0.94\lambda}{\beta \cos\theta} \quad (2.5)$$

Strain (ϵ): is the ratio of contraction or expansion in bonds lengths to the original bonds' lengths [37].

$$\epsilon = \frac{\beta}{4\tan\theta} \quad (2.6)$$

Dislocation density (δ): is a measure of the total length of dislocation lines per unit area [38].

$$\delta = \frac{15\epsilon}{aD} \text{ (lines/cm}^2\text{)} \quad (2.7)$$

Where a is the lattice constant in a-axis.

Stacking faults (SF): is a type of defects which characterizes the disordering of crystallographic planes. It is, thus, considered as planar defect [39].

$$SF = \frac{2\pi^2\beta}{45\sqrt{3}\tan\theta} \quad (2.8)$$

There is fourteen Bravais lattice in 3-dimensional that distributed in seven groups (structures) [40] represented in Table 2.2.

Table 2.2: The 3-D Bravais lattices for solid state materials and their conditions.

Crystal structure	Conditions	Number of Bravais Lattices
Triclinic	$a_1 \neq a_2 \neq a_3, \alpha \neq \beta \neq \gamma$	1
Monoclinic	$a_1 \neq a_2 \neq a_3, \alpha = \beta = 90^\circ \neq \gamma$	2
Orthorhombic	$a_1 \neq a_2 \neq a_3, \alpha = \beta = \gamma = 90^\circ$	4
Tetragonal	$a_1 = a_2 \neq a_3, \alpha = \beta = \gamma = 90^\circ$	2
Cubic	$a_1 = a_2 = a_3, \alpha = \beta = \gamma = 90^\circ$	3
Trigonal	$a_1 = a_2 = a_3, \alpha = \beta = \gamma < 120^\circ \neq 90^\circ$	1
Hexagonal	$a_1 = a_2 \neq a_3, \alpha = \beta = 90^\circ, \gamma = 120^\circ$	1

2.2 Optical Properties

The optical properties include the evaluation of transmittance, reflectance, absorption coefficient, energy gap, band tails and dispersion of dielectric constant. Fig. 2.2 presents the transmittance, reflectance and absorbance of light incident on optical medium.

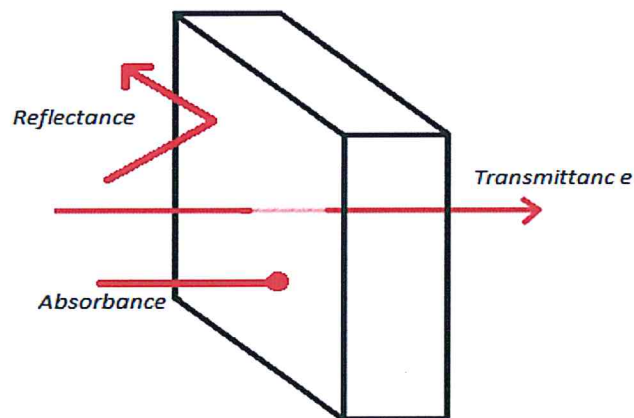


Fig2.2: The transmittance, reflectance and absorbance of light that incident on an optical medium.

2.2.1 Absorption coefficient

The absorption of light by an optical medium is determined by its absorption coefficient α . If the beam is propagating in the z direction, and the intensity at position z is $I(z)$, then the decrease of the intensity in an incremental slice thickness dz is given by:

$$dI = -\alpha dz I(z) \quad (2.9)$$

Integrate this to obtain Beer's law which state that:

$$I(z) = I_0 e^{-\alpha z} \quad (2.10)$$

Where z is the material thickness, I_0 is the optical intensity at $z=0$ and α is the absorption coefficient which is frequency dependent so this is the reason why material sometimes absorbed one color but not the other [41]. The transmissivity of the light in the medium of thickness l can be written as [41]:

$$T = (1 - R_1)(1 - R_2)e^{-\alpha l} \quad (2.11)$$

Where l is the thickness of the absorbing medium, R_1 and R_2 are the reflectance of the front and back layer of the medium and the term $(e^{-\alpha l})$ is the exponential decreased in the intensity because of the absorption according to Beer's law.

If R_1 and R_2 are equal, the equation becomes:

$$T = (1 - R)^2 e^{-\alpha l} \quad (2.12)$$

In the case of two materials deposited on the glass substrates we obtain:

$$T = (1 - R_1)(1 - R_2)(1 - R_3)e^{-\alpha l} \quad (2.13)$$

At $l = d$, the absorption coefficient is written as,

$$\alpha = -\frac{1}{d} \ln\left(\frac{T}{(1-R_1)(1-R_2)(1-R_3)}\right) \quad (2.14)$$

Particularly, in our work R_1 , R_2 and R_3 are the reflectance of glass, WO_3 and WO_3/Ga_2S_3 , respectively.

2.2.2 Tauc's Equation

The absorption coefficient is very important; In order to determine the energy gap of semiconductor and heterojunction, so Tauc's equation can be employed to determine the energy band gap which is can be written in the following formula [41- 43]:

$$(\alpha E)^{1/p} \propto (E - E_g) \quad (2.15)$$

Where α is the absorption coefficient, p takes the values 1/2, 3/2, 2, 3, corresponding to direct allowed, direct forbidden, indirect allowed and indirect forbidden transitions, respectively. E_g represents the energy gap. The derivation of Tauc's equation is shown in Appendix A.

2.2.3 Band Tails

The presence of Band tail is related to the exponential distribution of states in the band gap. That is found near the conduction and valance bands of disorder semiconductor.

In order to derive the relation between the absorption coefficient and band tails, suppose a p-type degenerate material [42], and the perturbed part of valence band lies above the Fermi level, so the density of initial state is proportional to $|E_v|^{1/2}$, where E_v is the energy state with respect to the edge of valence band, and the final state density from band tail to the conduction band as appear in the equation ,

$$N_f = N_i e^{\frac{E}{E_o}} \quad (2.16)$$

Where E_o is a parameter that describes the distribution of states but not their energy but has a dimension of the energy. The absorption coefficient is proportional to the product

of the final and initial state integrated all over the possible transition as appear in the following equation,

$$\alpha(h\nu) = A \int_{\xi_o}^{h\nu-\xi_o} |E_\nu|^{1/2} e^{-\frac{E}{E_o}} dE \quad (2.17)$$

Where A is constant

making change of variable to solve this integral

$$\text{let } x = \frac{h\nu-E}{E_o} \quad (2.18)$$

substituted x in the integral we obtain

$$\alpha(h\nu) = -A \exp\left(\frac{h\nu}{E_o}\right) (E_o)^{3/2} \int_{\frac{h\nu+\xi_o}{E_o}}^{\frac{\xi_o}{E_o}} x^{1/2} e^{-x} dx \quad (2.19)$$

because of $h\nu \gg E_o$, the lower limit of the integral can be set as ∞ then the solution can be written as

$$\alpha(h\nu) = A(E_o)^{3/2} e^{\frac{h\nu}{E_o}} \left[\frac{1}{2} (\pi)^{1/2} - \int_0^{\frac{\xi_o}{E_o}} x^{1/2} e^{-x} dx \right] \quad (2.20)$$

The slope of the absorption on the semi logarithmic plot gives

$$\left[\frac{d \ln \alpha}{d(h\nu)} \right]^{-1} = E_o \quad (2.21)$$

$$\frac{1}{E_o} = \frac{d \ln \alpha}{d(h\nu)} \quad (2.22)$$

Integrating both side of equation (2.22) yields

$$\frac{1}{E_o} \int d(h\nu) = \int d \ln(\alpha) \quad (2.23)$$

$$\ln \alpha = \alpha_o + \frac{hv}{E_o} \quad (2.24)$$

Where α_o is integration constant and hv is the photon energy (E)

Taking the exponential for both side of Eqn.(2.24) yields

$$\alpha = \alpha_o e^{\frac{E}{E_o}} \quad (2.25)$$

Plotting $\ln(\alpha)$ as a function of energy, the enter band energies can be determined from the slope.

2.2.4 The complex refractive index and dielectric constant

Dielectric constant(ϵ) or relative permittivity is the ratio of permittivity of material relative to the vacuum permittivity. Dielectric constant is a complex property that consists of real and imaginary parts. Where the refractive index (n) describes how fast light propagates through the medium, also n can be complex number. The derivation of the dielectric constant and the relation between the extinction coefficient and the absorption coefficient are shown in Appendix B [44, 45].

$$\epsilon_r = n^2 - K^2 \quad (2.26)$$

$$\epsilon_{im} = 2nK \quad (2.27)$$

$$K = \frac{\lambda \alpha}{4\pi} \quad (2.28)$$

2.2.5 Optical conductivity

The conductivity as a function of frequency can be determined from the imaginary part of dielectric constant and the frequency of the light. The dielectric is complex function and then the conductivity is also complex. We derive it by starting with Maxwell's Equations (C.G.C units) [44]:

$$\nabla \times \mathbf{H} - \frac{1}{c} \frac{\partial \mathbf{D}}{\partial t} = \frac{4\pi}{c} \mathbf{j} \quad (2.29)$$

$$\nabla \times \mathbf{E} + \frac{1}{c} \frac{\partial \mathbf{B}}{\partial t} = 0 \quad (2.30)$$

$$\nabla \cdot \mathbf{D} = 0 \quad (2.31)$$

$$\nabla \cdot \mathbf{B} = 0 \quad (2.32)$$

Where we have assumed that the charge density is zero.

$$\mathbf{D} = \varepsilon \mathbf{E} \quad (2.33)$$

$$\mathbf{B} = \mu \mathbf{H} \quad (2.34)$$

$$\mathbf{j} = \sigma \mathbf{E} \quad (2.35)$$

From Maxwell's equations and the above equations, we obtain the wave equations for the fields \mathbf{E} and \mathbf{H} :

$$\nabla^2 \mathbf{E} = \frac{\varepsilon \mu}{c^2} \frac{\partial^2 \mathbf{E}}{\partial t^2} + \frac{4\pi \sigma \mu}{c^2} \frac{\partial \mathbf{E}}{\partial t} \quad (2.36)$$

$$\nabla^2 \mathbf{H} = \frac{\varepsilon \mu}{c^2} \frac{\partial^2 \mathbf{H}}{\partial t^2} + \frac{4\pi \sigma \mu}{c^2} \frac{\partial \mathbf{H}}{\partial t} \quad (2.37)$$

The solution of Eqns. (2.36) and (2.37) is sinusoidal:

$$\mathbf{E} = \mathbf{E}_0 e^{i(\mathbf{K} \cdot \mathbf{r} - \omega t)} \quad (2.38)$$

Where \mathbf{K} is a complex propagation constant and ω is the frequency of the light. The same solution for the \mathbf{H} field. The real part of \mathbf{K} can be identified as a wave vector, where the imaginary part accounts for attenuation of the wave inside the solid.

Substitute the plane wave solution Eqn. (2.38) into the wave equation Eqn. (2.36) yields:

$$-\mathbf{K}^2 = -\frac{\varepsilon \mu \omega^2}{c^2} - \frac{4\pi i \sigma \mu \omega}{c^2} \quad (2.39)$$

If there is no losses or attenuation, \mathbf{K} would be equal to

$$\mathbf{K}_0 = \frac{\omega}{c} \sqrt{\varepsilon \mu} \quad (2.40)$$

and would be real, but since there are losses so write

$$K = \frac{\omega}{c} \sqrt{\epsilon_{complex} \mu} \quad (2.41)$$

Where we have defined the complex dielectric function as

$$\epsilon_{complex} = \epsilon + \frac{4\pi i \sigma}{\omega} = \epsilon_1 + i\epsilon_2 \quad (2.42)$$

ϵ_1 and ϵ_2 represents the real and imaginary parts of dielectric, respectively.

$$\epsilon_2 = \epsilon_{im} = \frac{4\pi\sigma}{\omega} \quad (2.43)$$

$$\text{So, } \sigma(\omega) = \frac{\omega \epsilon_{im}}{4\pi} \quad (2.44)$$

2.3 Electrical properties

2.3.1 Current Conduction Mechanisms

In metal-semiconductor contact (schottky barrier) there are several current mechanisms that contribute to the transport of the minority or majority carriers through barrier of the device, most of these mechanisms causes the flow of carriers in forward direction and other in the reverse direction. These types are Thermionic Emission, Generation-Recombination process, diffusion current and quantum tunneling of electrons [46, 47].

2.3.1.1 Thermionic emission current

It is a majority carrier currents and is always associated with a potential barrier. The most common device is the Schottky-barrier or metal-semiconductor junction. Thermionic emission over the barrier determines the current transport of schottcky contacts with moderate doping levels of the semiconductors [48]. The thermionic emission theory is derived from these assumptions:

- (1) The barrier height $q\phi_{Bn}$ is much larger than kT .
- (2) Thermal equilibrium is established at the plane that determines emission.

- (3) The existence of a net current flow does not affect this equilibrium so that one can super impose two currents fluxes-one from the metal to semiconductor and the other from semiconductor to metal; each has different quasi Fermi level [47].

The current flow does not depend on the shape of barrier but it only barrier height dependence.

The current density from the semiconductor to the metal $J_{s \rightarrow m}$ is given by [47]:

$$J_{s \rightarrow m} = \int_{E_{Fn} + q\phi_{Bn}}^{\infty} q v_x dn \quad (2.45)$$

Where $E_{Fn} + q\phi_{Bn}$ is the minimum energy needed for thermionic emission into the metal, and v_x is the carrier velocity in the direction of transport (x-direction). The density of energy is

$$dn = N(E)F(E)dE \quad (2.46)$$

$$\approx \frac{4\pi(2m^*)^{3/2}}{h^3} \sqrt{E - E_c} \exp\left(-\frac{E - E_c + q\phi_n}{kT}\right) dE \quad (2.47)$$

where $N(E)$ and $F(E)$ are the density of states and the distribution function, respectively.

If all the energy of electrons in the conduction band is kinetic energy, then,

$$E - E_c = \frac{1}{2} m^* v^2 \quad (2.48)$$

$$dE = m^* v dv \quad (2.49)$$

$$\sqrt{E - E_c} = v \sqrt{\frac{m^*}{2}} \quad (2.50)$$

Substitute Eqns. (2.48), (2.49) and (2.50) in Eqn. (2.47) gives

$$dn \approx 2 \left(\frac{m^*}{h}\right)^3 \exp\left(-\frac{q\phi_n}{kT}\right) \exp\left(-\frac{m^* v^2}{2kT}\right) (4\pi v^2 dv) \quad (2.51)$$

This equation gives the number of electrons per unit volume that have velocities between v and $v + dv$, in all directions. But

$$v^2 = v_x^2 + v_y^2 + v_z^2 \quad (2.52)$$

With the transformation $4\pi v^2 dv = dv_x dv_y dv_z$

We obtain from equations (2.45), (2.51) and (2.52) obtain

$$\begin{aligned}
 J_{s \rightarrow m} &= 2 q \left(\frac{m^*}{h} \right)^3 \exp\left(-\frac{q\phi_n}{kT}\right) \int_{v_{0x}}^{\infty} v_x \exp\left(-\frac{m^* v_x^2}{2kT}\right) dv_x \int_{v_{0y}}^{\infty} v_y \exp\left(-\frac{m^* v_y^2}{2kT}\right) dv_y \\
 &\quad \int_{v_{0z}}^{\infty} v_z \exp\left(-\frac{m^* v_z^2}{2kT}\right) dv_z \\
 &= \left(\frac{4\pi q m^* k^2}{h^3} \right) T^2 \exp\left(-\frac{q\phi_n}{kT}\right) \exp\left(-\frac{m^* v_{0x}^2}{2kT}\right)
 \end{aligned} \tag{2.53}$$

The velocity v_{0x} is the minimum velocity required in the x-direction to surmount the barrier and is given by ψ

$$\frac{1}{2} m^* v_{0x}^2 = q(\psi_{bi} - V) \tag{2.54}$$

Substituting Eqn. (2.54) in Eqn. (2.53) yields

$$\begin{aligned}
 J_{s \rightarrow m} &= \left(\frac{4\pi q m^* k^2}{h^3} \right) T^2 \exp\left(-\frac{q\phi_{Bn}}{kT}\right) \exp\left(\frac{qV}{kT}\right) \\
 &= A^* T^2 \exp\left(-\frac{q\phi_{Bn}}{kT}\right) \exp\left(\frac{qV}{kT}\right)
 \end{aligned} \tag{2.55}$$

$$A^* = \left(\frac{4\pi q m^* k^2}{h^3} \right)$$

Which is the effective Richardson constant for thermionic emission.

The current from metal into the semiconductor is equal to the current from the semiconductor into the metal when thermal equilibrium is achieved ($V = 0$).

The corresponding current density is determined by setting $V = 0$

$$J_{m \rightarrow s} = -A^* T^2 \exp\left(-\frac{q\phi_{Bn}}{kT}\right) \tag{2.56}$$

The total current is given by the sum of Eqn.(2.55) and (2.56)

$$J_n = A^* T^2 \exp\left(-\frac{q\phi_{Bn}}{kT}\right) \left[\exp\left(\frac{qV}{kT}\right) - 1 \right] \tag{2.57}$$

$J = I/A$, Then the current is:

$$I = AA^* T^2 \exp\left(-\frac{q\phi_B}{kT}\right) \exp\left(\frac{qV}{\eta kT}\right) \quad (2.58)$$

Where η is the ideality factor, the exponential qV/kT is larger than 1, so that the number 1 can be deleted. When assuming series resistance effect, $-IR_s$ term added to the exponential. Then, we obtain

$$I = AA^* T^2 \exp\left(-\frac{q\phi_B}{kT}\right) \exp\left(\frac{qV-IR_s}{\eta kT}\right) \quad (2.59)$$

2.4 Capacitance (C)-Voltage (V) characteristics

In addition to the Current (I)-Voltage (V) measurements the Capacitance (C)-Voltage (V) characteristics is also measured due to the important device parameters that can obtain. The C-V characteristic of the MOS structure is perhaps the most frequently used tool in the characterization of both the MOS and the MOSFET devices [49]. In this technique a small AC signal was superimposed on the DC bias, so the capacitance will depend on the frequency [46]. C-V measurements can be used to study impurity levels, and the built in voltage for the device.

Let assume we have contact on n-type semiconductor under abrupt approximation that $\rho = qN_D$, for $x < W_D$, $\rho = 0$ and $E = 0$ for $x > W_D$ where ρ is the charge density and W_D is the depletion width [47], we obtain

$$W_D = \sqrt{\frac{2\varepsilon_s}{qN_D} \left(V_{bi} - V - \frac{kT}{q} \right)} \quad (2.60)$$

$$|E(x)| = \frac{qN_D}{\varepsilon_s} (W_D - x) = E_m - \frac{qN_D x}{\varepsilon_s}$$

$$E_c(x) = q\phi_{Bn} - \frac{q^2 N_D}{\varepsilon_s} \left(W_D x - \frac{x^2}{2} \right) \quad (2.61)$$

Where E_m is the maximum field, $q\phi_{Bn}$ is the built in voltage for n-type semiconductor, N_D is the donor density, ϵ_s is the semiconductor dielectric constant and W_D is the depletion width.

$$E_m = E(x=0) = \sqrt{\frac{2qN_D}{\epsilon_s} \left(V_{bi} - V - \frac{kT}{q} \right)} = \frac{2[V_{bi} - V - (kT/q)]}{W_D} \quad (2.62)$$

The space charge per unit area is given by

$$Q_{sc} = qN_D W_D = \sqrt{2q\epsilon_s N_D \left(V_{bi} - V - \frac{kT}{q} \right)} \quad (2.63)$$

The depletion layer capacitance per unit area is

$$C_D = \frac{\epsilon_s}{W_D} = \frac{q\epsilon_s N_D}{\sqrt{2[V_{bi} - V - (kT/q)]}} \quad (2.64)$$

Eqn.(2.64) can be written in the form [48]

$$\frac{1}{C_D^2} = \frac{2[V_{bi} - V - (kT/q)]}{q\epsilon_s N_D} \quad (2.65)$$

Plotting $1/C_D^2$ versus voltage a straight line is obtained if N_D is constant through the depletion region. if N_D is not constant, the differential capacitance method can be used to determine the doping profile.

2.5 RLC circuits

An electrical circuit (RLC) consists of a resistor (R), an inductor (L), and a capacitor (C), these components are connected in series or parallel. In RLC an AC signal is provided by the source voltage on the circuit.

2.5.1 The series RLC circuits

The magnitude of the source voltage (V_s) is made up of the three individual element voltages, V_L , V_R and V_C , while the current of each component being the same in amplitude. Fig. 2.3 shows the series LRC circuit.

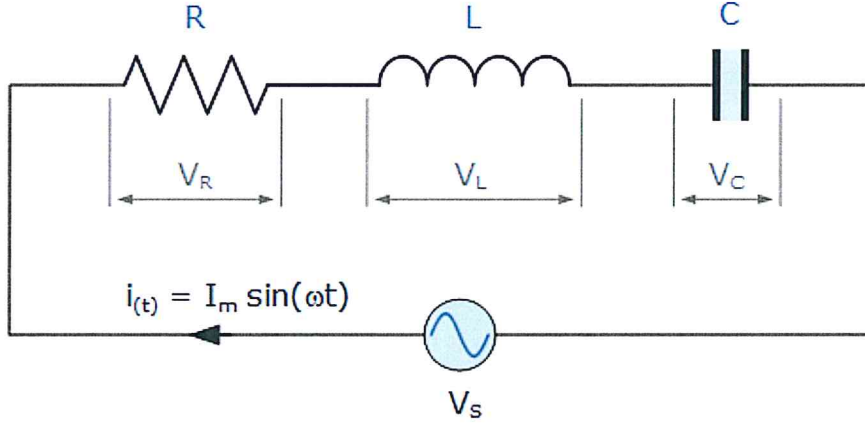


Fig. 2.3: The series RLC circuit diagram.

The source voltage is given by:

$$V_L = I\omega L, V_R = IR, V_C = \frac{I}{\omega C} \quad (2.66)$$

By applying Kirchhoff's voltage law [50], getting:

$$V_s = IR + L \frac{dI}{dt} + \frac{Q}{C} \quad (2.67)$$

Voltage triangle for a series RLC circuit gives that:

$$V_s = \sqrt{V_R^2 + (V_L - V_C)^2} = I\sqrt{R^2 + (X_L - X_C)^2} = IZ \quad (2.68)$$

The amplitude of the source voltage is proportional to the amplitude of the current with proportionality constant called the impedance of the circuit. The overall impedance depends on the resistance and the inductive and capacitive reactance of the circuit by the relation which can be represented by an impedance triangle as shown in Fig. 2.4 [51].

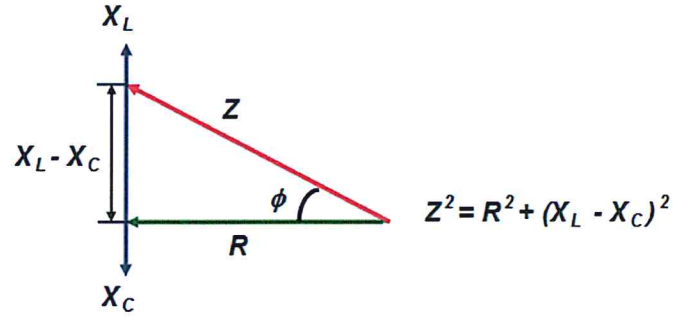


Fig. 2.4: The impedance triangle of series RLC circuit.

2.5.2 The parallel RLC circuits

The source voltage is the same for all three components whereas the supply current I_s will be the vector sum of the three individual branch currents I_L , I_R and I_C . This circuit is shown in Fig. 2.5.

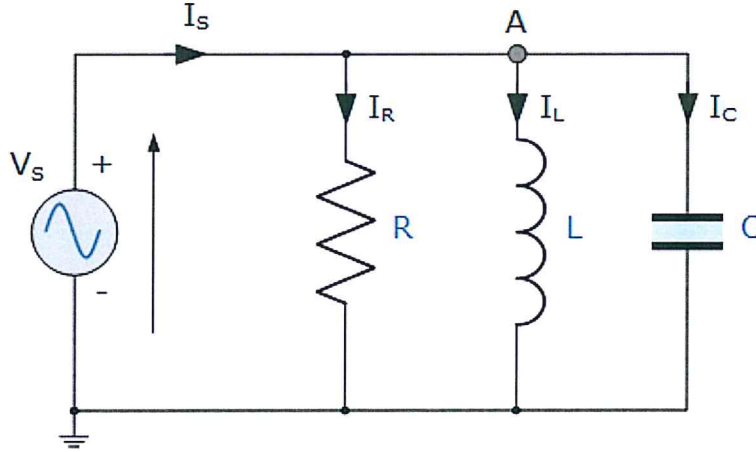


Fig. 2.5: The parallel RLC circuit diagram.

The current through each branch is found by applying Kirchhoff's Current Law [50] again,

$$I_s = \frac{1}{RC} \frac{dV}{dt} + \frac{V}{LC} + C \frac{d^2V}{dt^2} \quad (2.69)$$

By the current triangle we get

$$I_s = \sqrt{I_R^2 + (I_L - I_C)^2} = \sqrt{\left(\frac{V}{R}\right)^2 + \left(\frac{V}{X_L} - \frac{V}{X_C}\right)^2} = \frac{V}{Z} \quad (2.70)$$

$$\text{Where } I_R = \frac{V}{R}, I_L = \frac{V}{X_L}, I_C = \frac{V}{X_C} \quad (2.71)$$

The combination of X_L , X_C and R gives the circuit impedance Z by the relation:

$$Z = \frac{1}{\sqrt{\left(\frac{1}{R}\right)^2 + \left(\frac{1}{X_L} - \frac{1}{X_C}\right)^2}} \quad (2.72)$$

It is seen that both of the series and parallel RLC circuits contain inductive reactance and capacitive reactance within the same circuit. When the frequency varies across circuits there must be a point where a minimum impedance takes place ($Z=R$). The frequency at which this condition is satisfied is called resonant frequency.

2.5.3 The return loss

The return loss is a measure of the power that is not dissipated by the load and is returned to the source. The higher the absolute value of the return loss (i.e.: $> |20|$ dB) the better the match. The return loss (expressed in dB) makes use of ρ to be [52]:

$$Lr = -20 \log(\rho) \quad (2.73)$$

Here, ρ represents the amplitude of the reflection coefficient spectra and calculated from the relation,

$$\rho = \frac{Z_{load} - Z_{source}}{Z_{load} + Z_{source}} \quad (2.74)$$

In a matched load $\rho=0$ and return loss is ∞ ; in a mismatched load, $\rho=1$ return loss is 0 dB, and in this case an open circuit is presented.

Chapter Three

Experimental details

In order to fabricate electronic devices, thin films should be prepared. Different methods can be used to prepare thin films as mentioned previously. In this work, the technique we used is the thermal vapor deposition technique.

3.1 Cleaning glass

In this method cleaned glass (Soda Lime; $\text{SiO}_2\text{:Na}_2\text{O:MgO:CaO}$) must be used as a substrate in order to get tidy and obvious samples. Firstly, a 2.5 cm-length glass substrates were washed by distilled water. Then immersed with 70%-Ethyl-Alcohol and covered with aluminum foil. Heating the ultrasonic resonator to 70 °C for 20 min, the ultrasonically cleaned glass is taken immersed and washed with alcohol then dried using hair dryer and glass paper. It is necessary to check that the cleaned glass has no scratch on the surface to avoid production of rough surface.

3.2 Evaporating process and thin film preparations

The ultrasonically-cleaned glass was sorted on the metal plate close to each other, the evaporation process was done for 5 times to design our device using VCM 600 evaporation system under vacuum at 5×10^{-5} mbar. Fig. 3.1 shows the evaporation system.



Fig. 3.1: The 600 VCM evaporation system.

The first step was the evaporating of Ytterbium metal. A 0.2-g of Yb metal was evaporated and a $1.0\ \mu\text{m}$ is deposited onto the glass. TEFLON tape is used to cover small region (about 2 mm) on the edges of Yb-substrate before depositing Tungsten oxide. The second run, required using glass-substrate in addition to Yb-substrate. A 0.2-g of WO_3 was evaporated and a layer of $1.0\ \mu\text{m}$ WO_3 film was deposited on the glass and Yb-substrates. To establish two channels, TEFLON was used again to cover half the surface of produced samples to evaporate Gallium Sulfide. The same amount of 0.2 g Ga_2S_3 was evaporated onto glass, Yb, WO_3 and Yb/ WO_3 substrates and $1.0\ \mu\text{m}$ -thick Ga_2S_3 was deposited. The produced thin films were WO_3 , Ga_2S_3 , $\text{WO}_3/\text{Ga}_2\text{S}_3$, Yb/ WO_3 , Yb/ Ga_2S_3 , Yb/ $\text{WO}_3/\text{Ga}_2\text{S}_3$ films.

In the case of electronic devices two metal terminals were needed, the Yb-substrate was necessary for I-V and Impedance measurements, the other is needed so evaporation process should take place. Using TEFLON, four point contacts ($7.84 \times 10^{-3} \text{ cm}^2$) on each channel (Yb/ WO_3 and Yb/ $\text{WO}_3/\text{Ga}_2\text{S}_3$) were produced. Two points related to the evaporation of $1.0 \mu\text{m}$ Yb and the others related to evaporation of $1.0 \mu\text{m}$ Au metal. The final prepared films are shown in Fig. 3.2.

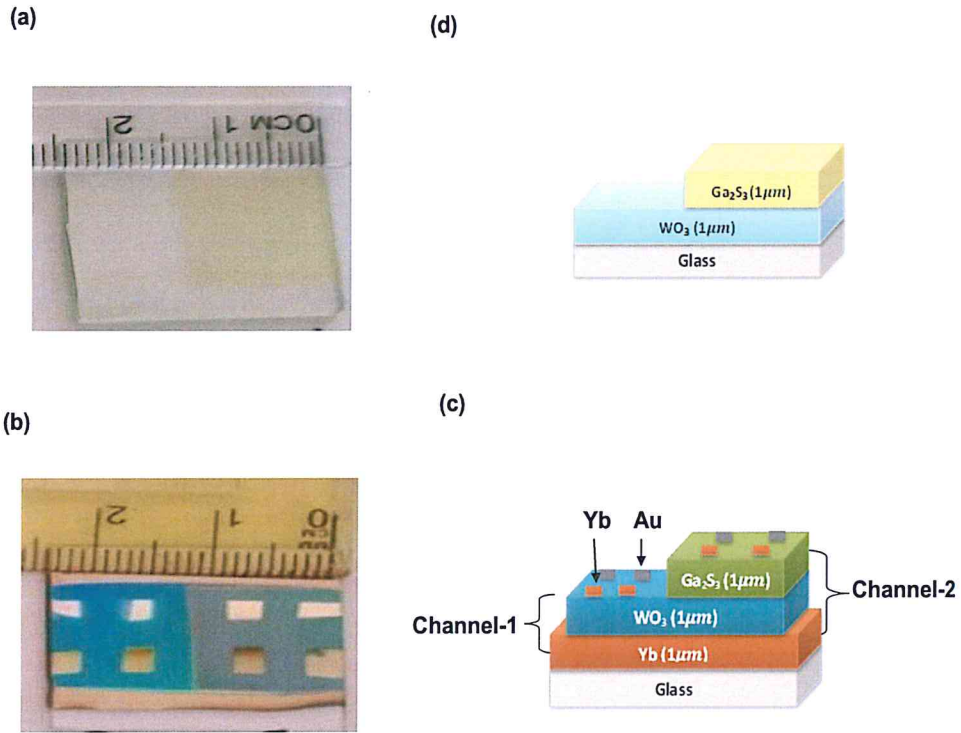


Fig. 3.2: The prepared thin films (a) and (b) experimentally (c) and (d) geometrical design.

3.3 Thin Film analysis

Properties of the prepared films such as, structural, optical and electrical are investigated by the techniques in the following sections.

3.3.1 The X-ray diffraction (XRD) measurements

The crystalline structure of WO_3 , Ga_2S_3 and $\text{WO}_3/\text{Ga}_2\text{S}_3$ thin films were detected by means of Rigaku diffractometer equipped with $\text{K}\alpha$ radiation of a copper anode of average wavelength of 1.5405 \AA at 40 KV and 15 mA. The Rigaku diffractometer is displayed in Fig. 3.3. The 2θ was set between 10° - 70° with scan speed 1 deg/min. The schematic diagram of XRD is presented in Fig. 3.4.



Fig. 3.3:X-ray Rigaku diffractometer.

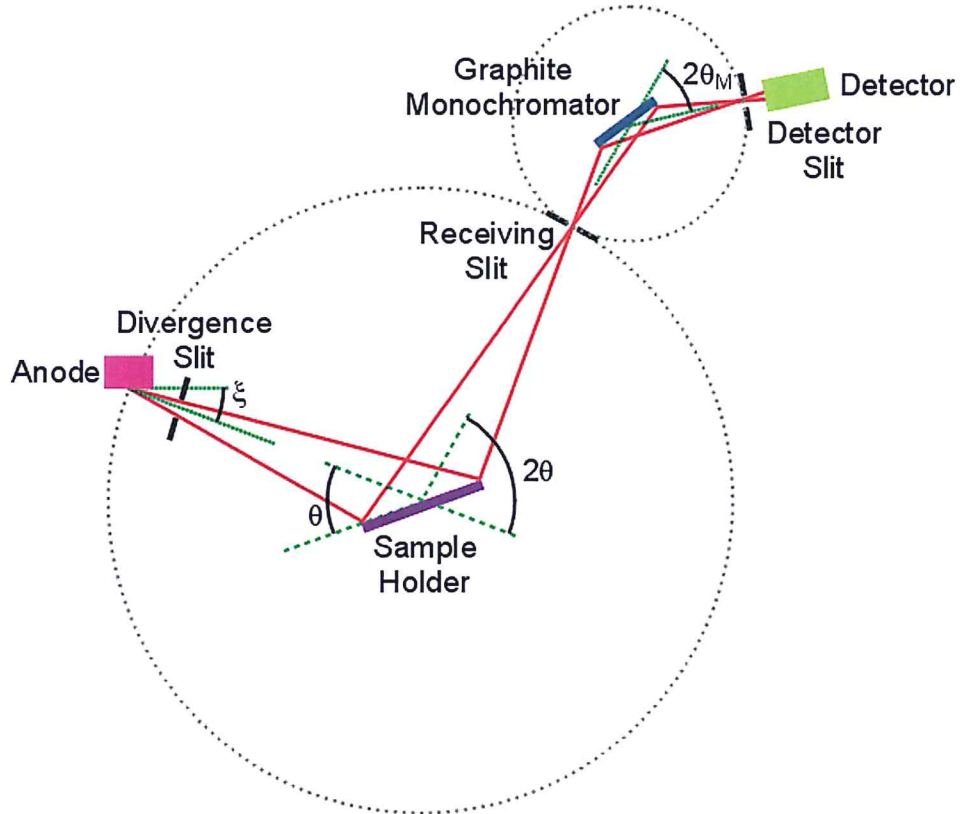


Fig. 3.4: The schematic diagram of XRD.

3.3.2 Scanning Electron Microscopy (SEM) measurements

Scanning electron microscopy was used to produce images of our samples by scanning the surface with beam of electrons. The interaction between the electron beam and the atoms in the sample producing signals that contain information about the shape and features of the surface and the composition of the samples.

The images of samples were taken by the SEM in our lab with 1K, 100K and 300K enlargements for three regions including WO_3 , Ga_2S_3 and $\text{WO}_3/\text{Ga}_2\text{S}_3$. Fig. 3.5 shows the schematic diagram of SEM.

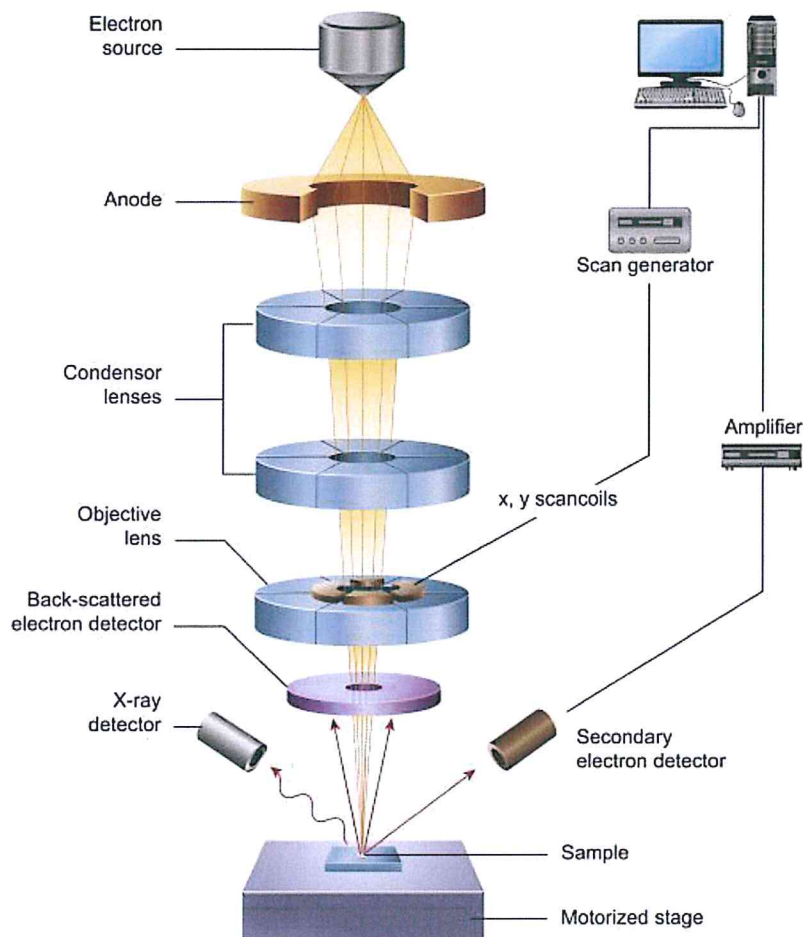


Fig. 3.5: The schematic diagram of SEM.

3.3.3 Energy-dispersive X-ray spectroscopy (EDX)

The energy-dispersive X-ray analyzer attached to the SEM system can be used to record the atomic contents. In this technique, the composition of the sample elements is determined depending on the X-ray generation in which a unique set of characteristic X-ray for each element is produced and sorted depending on its energy.

The composition of WO_3 , Ga_2S_3 and $\text{WO}_3/\text{Ga}_2\text{S}_3$ films were studied using EDX.

3.3.4 Optical Measurements

WO_3 , Ga_2S_3 and $\text{WO}_3/\text{Ga}_2\text{S}_3$ films were subjected to optical measurements by means of Evolution 300 Ultra Violet visible light spectrophotometer as displayed in Fig.3.6. The transmittance and reflectance are measured in the wavelength range 300-1100 nm where the scan speed 1200 nm/min. The data is analyzed using Vision Pro program. Depending on the transmittance and reflectance, the energy gaps, interband transition energies, dielectric constant and optical conductivity are determined.

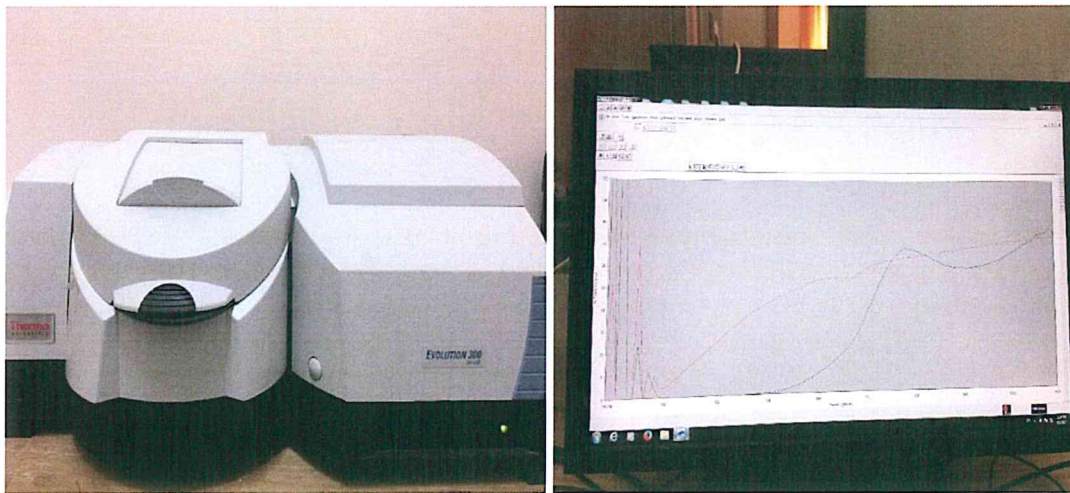


Fig. 3.6: The UV-VIS spectrophotometer.

3.3.5 The hot-probe technique

The types of semiconductors are important particularly when we design the energy band gap diagram. The hot-probe technique is used to recognize the conductivity type of semiconductors. In this technique digital multi-meter (DMM) and heater were used, in which the hot iron was connected to the positive terminal of the DMM and the cold iron was connected to the negative terminal. When the DMM reads negative voltage, the

semiconductor is p-type. In contrast, n-type semiconductor requires reading positive voltage on the multi-meter. Fig. 3.7 displays the set-up of hot-probe technique.

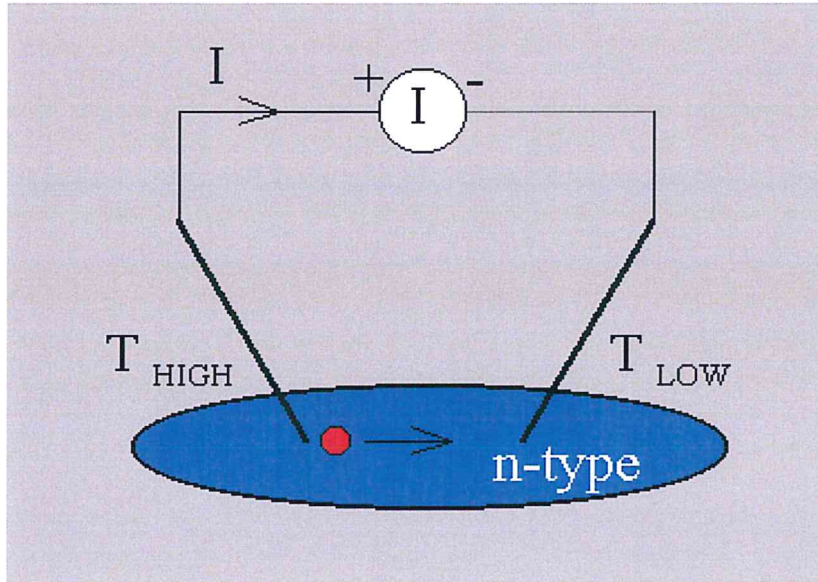


Fig. 3.7: The set-up of hot-probe technique.

3.3.6 Impedance Measurements

To measure the impedance of the thin films, an Ac signal is provided by Agilent 4291BRF signal Generator impedance analyzer (10 -1800MHz) spectrometer which is shown in Fig. 3.8.

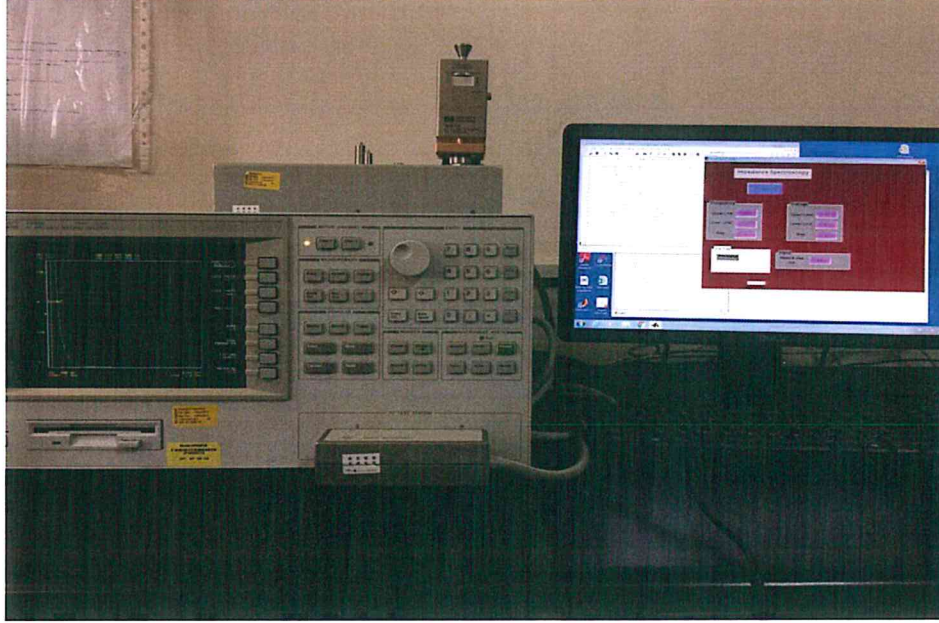


Fig. 3.8: The set-up for impedance measurements using Agilent 4291B RF Signal Generator impedance analyzer.

The measured impedance (Z) is composed from resistive and reactive parts, the reactive part including capacitance (C) and inductance (L). In our experiment, the series and parallel capacitance, Conductance, impedance and reflection coefficient were measured in the frequency range 10-1800 MHz where the signal was recorded with the help of MATLAB software.

3.3.7 The Current-Voltage Measurements

The current-voltage measurements can be recorded in a sandwiched structure with two metal contacts on the opposite sides of the thin films. In our films, we have different terminals Yb (bottom) and Au (top) for both channels WO_3 and $\text{WO}_3/\text{Ga}_2\text{S}_3$. Also, similar terminals in which the films registered between two contacts of Yb (in the top and bottom). The measurements of current-voltage were determined using a computerized Keithley 6485 picoammeter and a Keithley 230 voltage source in the dark. The Model

6485 Picoammeter has of high sensitivity to measure currents less than 1.0 nA. At higher currents, this device makes accurate current measurements. Also, the MATLAB software was used to collect the data from the devices. In this part, different relations between the current and voltage are plotted and determined that helps to calculate important electrical parameters of the devices. All measurements are done at room temperature.

Chapter four

Results and discussions

4.1 Structural analysis

Tungsten oxide (WO_3), Gallium Sulfide (Ga_2S_3) and $\text{WO}_3/\text{Ga}_2\text{S}_3$ thin films of thicknesses of $1.0\ \mu\text{m}$, $1.0\ \mu\text{m}$ and $2.0\ \mu\text{m}$, respectively, are deposited onto glass substrates were investigated by X-ray diffraction technique (XRD) in order to identify their crystal structure. The resulting X-ray diffraction patterns for the optical image which is shown in the inset-1 of Fig. 4.1 are displayed in the same figure.

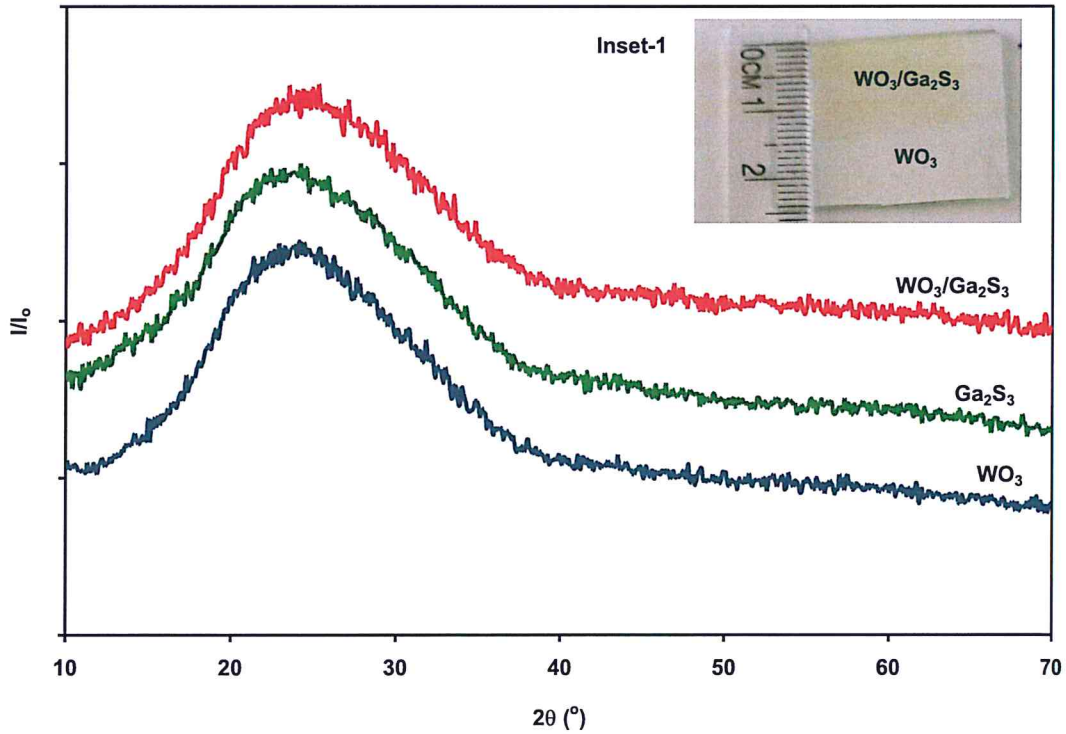


Fig. 4.1: The X-ray diffraction patterns for $1.0\ \mu\text{m}$ WO_3 , $1.0\ \mu\text{m}$ Ga_2S_3 and $2.0\ \mu\text{m}$ $\text{WO}_3/\text{Ga}_2\text{S}_3$ films deposited onto glass substrates.

The figure shows no remarkable peaks in the XRD patterns when the samples were deposited onto glass substrates indicating the amorphous nature of the studied samples. This amorphous nature of WO_3 is due to the polymorphic phases of WO_3 which is reported to be temperature dependent [53]. The possible phases of WO_3 are triclinic form which can be obtained at -50 to 17°C , monoclinic exists in the range of 17 to 330°C , orthorhombic is obtained above 330 to 740°C , tetragonal phase is achieved at temperature above 740°C and cubic phase. The most common structure of WO_3 is monoclinic with space group $\text{P2}_1/\text{n}$ [2]. In another work, a similar amorphous structural behavior was detected in WO_3 and was assigned to the topology. It is found that there is a temperature range where this material forms microcrystalline states [54]. Similarly, for Ga_2S_3 films the amorphous structure was observed. The polymorphic phases for Ga_2S_3 are the main reason for the noncrystalline nature [55]. Cubic zincblend type ($\gamma\text{-Ga}_2\text{S}_3$), hexagonal wurtzite type ($\beta\text{-Ga}_2\text{S}_3$) and monoclinic wurtzite type ($\alpha\text{-Ga}_2\text{S}_3$) phases of Ga_2S_3 are formed at growth temperatures of 873 K , 820 K and 1020 K , respectively [22]. While α phase is of ordered vacancy, the β and γ phases are of highly disordered vacancies [22, 56]. Namely, in the preparation of Ga_2S_3 thin film the temperature is increased until reach the melting temperature, at this temperature the melt is composed of all phases (α , β and γ). Each phase has different thermal energy and different equilibrium temperature than the other phases. This leads to the formation of clusters of various phases localized at the surface of thin film indicating the amorphous structure as observed. Moreover, it is reported that the surface defects can be a reason for the amorphous structure of Ga_2S_3 [56]. The XRD patterns for Ga_2S_3 were measured through preparing of $\text{Ga}_2\text{S}_3/\text{In}/\text{Ga}_2\text{S}_3$ and a similar noncrystalline phase was detected [57]. The

WO₃/Ga₂S₃ interfaces also exhibited the amorphous structure which is due to the deposition of two amorphous layers.

The XRD patterns of WO₃, Ga₂S₃ and WO₃/Ga₂S₃ films grown onto Yb substrates are shown in Fig. 4.2. The crystalline nature of the studied films was investigated using "Crystal diffraction" software. Three peaks are observed for Yb/WO₃ films. The most intensive peak appears at $2\theta = 28.3^\circ$ being reflected from planes oriented in the (111) direction, while the minor peaks occurring at $2\theta = 25.4^\circ$ and 32.1° are assigned to planes oriented in the (011) and (111) directions. The most intensive one related to the cubic structure of Yb which has lattice constant $a = 5.370 \text{ \AA}$ [58]. Whereas, the minor peak of (011) orientation is assigned to orthorhombic structure of WO₃ [20] and the other peak of (111) orientation is ascribed to tetragonal WO₃ structure [21]. Using Yb metal as a substrate induced the crystallization of WO₃ films and then different peaks are observed.

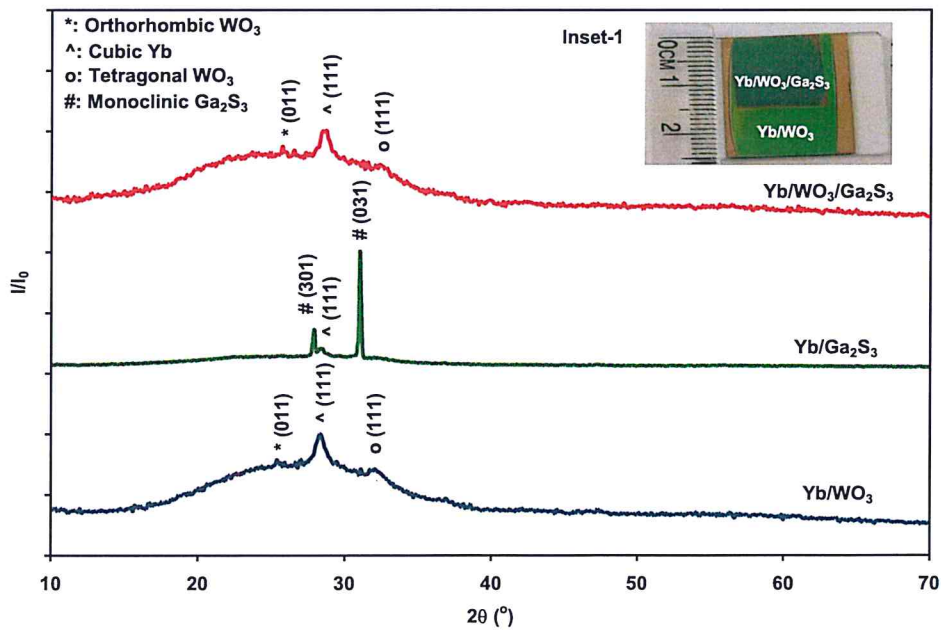


Fig. 4.2: The X-ray diffraction patterns for WO₃, Ga₂S₃ and WO₃/Ga₂S₃ films deposited onto Yb substrates.

On the other hand, depositing Ga_2S_3 onto Yb metal substrate reveals crystalline phase of Yb/ Ga_2S_3 films. Three peaks appeared in Fig. 4.2. The most sharp peak located at $2\theta = 31.0^\circ$ which is directed in the (031) plane is assigned to the monoclinic Ga_2S_3 structure (α - Ga_2S_3) [22]. The peak located at $2\theta = 27.9^\circ$ is oriented in the direction of (301) also returns to the same phase structure of Ga_2S_3 . The least intensive peak which was detected at $2\theta = 28.5^\circ$ are related to the cubic structure of ytterbium. In the case of Yb/ WO_3 / Ga_2S_3 three peaks are also observed. The most intensive peak appears at $2\theta = 28.7^\circ$ in the direction of (111) and is assigned to cubic Yb structure [58]. The second peak locates at $2\theta = 25.7^\circ$ in the direction of (011) where it is ascribed to the orthorhombic WO_3 structure [20]. The third peak which locates at $2\theta = 32.5^\circ$ oriented in the (111) direction is assigned to tetragonal WO_3 structure [21] as tabulated in Table 4.1.

On my think that, the reason for induced crystallization is may be assigned to the strong Coulombic interactions between Yb-O. The bond length of Yb-O is 2.51 Å [59] and for W-O is 1.799 Å, so the Coulombic interactions between W-O is stronger than that of Yb-O which is not probable reason for induced crystallization. Another reason for crystal formation is strained structure which is increased with lattice mismatch between Yb and WO_3 films.

The grain size, microstrain, dislocation density and stacking faults were calculated with the help of Eqns. (2.5), (2.6), (2.7) and (2.8), respectively. The peak for orthorhombic WO_3 which is observed at $2\theta = 25.4^\circ$ is shifted to the right at $2\theta = 25.7^\circ$ upon coating of Ga_2S_3 , the grain size represented by the peak is found to decrease from 67 to 60 nm upon coating of Ga_2S_3 onto the surface of WO_3 . While, the microstrain, dislocation density and

stacking faults are increased from 2.46×10^{-3} to 2.74×10^{-3} , from 7.46×10^{10} to 9.33×10^{10} (lines/cm²) and from 0.118% to 0.132% , respectively, as presented in Table 4.2.

Recalling that the ionic radiuses of Ga⁺³, W⁺⁶, S⁻² and O⁻² are 62 [60], 60 [61], 184 [62] and 140 [63] pm, respectively. It is possible to think that the coating of Ga₂S₃ onto WO₃ may lead to vacancy filling process. Namely, vacant sites in W may be filled with Ga owing to the very closes radiuses of the ions. In addition, excess surface oxygen atoms in WO₃ may interact with Ga atoms to fill empty sites of sulfur. The idea is supported through considering the bond lengths of the reagents. Particularly, as the bond lengths of Ga-S being 2.32 Å [32], that of Ga-O is 1.84 Å [64], the bond length of W-O is 1.799 Å [65] and the bond length of W-S is 2.41 Å [66], then the coulombic interactions between Ga and O is stronger than that of Ga and S atoms this make interactions between Ga and oxygen atoms more preferable than that of W and S atoms. On the other hand, since the coulombic forces between W and O is stronger than that between W and S, interactions between these two ions to form WS₃ is excludable. The formation of Ga₂O₃ at the ultrathin interface between WO₃ and Ga₂S₃ leads to strained structure. Strained structures leads to the attenuation in the structural parameters. Usually elastic and inelastic deformations that leads to structure deflection at the micro-level take place [67]. These kinds of interactions could also be assigned as a reason for the induced crystallization of the studied materials.

Table 4.1: A structural comparison between the stacked layers of Yb/WO₃, Yb/Ga₂S₃ and Yb/WO₃/Ga₂S₃.

Peaks	Yb/WO ₃			Yb/Ga ₂ S ₃			Yb/WO ₃ /Ga ₂ S ₃		
	2 θ	Plane	Structure	2 θ	Plane	Structure	2 θ	Plane	Structure
1 st peak	25.4°	(011)	Orth. WO ₃	27.9°	(301)	Mono. Ga ₂ S ₃	25.7°	(011)	Orth. WO ₃
2 nd peak	28.3°	(111)	Cubic Yb	28.5°	(111)	Cubic Yb	28.7°	(111)	Cubic Yb
3 rd peak	32.1°	(111)	Tetra. WO ₃	31.0°	(031)	Mono. Ga ₂ S ₃	32.5°	(111)	Tetra. WO ₃

Table 4.2: The structural parameters of WO₃ and WO₃/Ga₂S₃ thin films.

Samples	2 θ	I	d (nm)	D(nm)	$\varepsilon (\times 10^{-3})$	δ (lines/cm ²) $\times 10^{10}$	SF%
Yb/WO ₃	25.4°	4049	0.35	67	2.46	7.46	0.118%
Yb/WO ₃ /Ga ₂ S ₃	25.7°	3297	0.35	60	2.74	9.33	0.132%

Fig.4.3 displays the scanning electron microscopy images which were recorded from the surface of the $\text{WO}_3/\text{Ga}_2\text{S}_3$ films. The collected images of the surface of the interface are shown in Fig. 4.3 (a), (b) and (c) for magnified at 1K, 100K and 300K times, respectively. An amorphous nature is observed on the surface of $\text{WO}_3/\text{Ga}_2\text{S}_3$ and WO_3 , no grains are appeared in the figures. These results agree with the X-ray analysis which exhibits the same structural property. One interesting feature of the shown images appears at the $\text{WO}_3/\text{Ga}_2\text{S}_3$ boundary. Even at the nanoscale level of measurement as shown in Fig. 4.3 (c), the boundary is highly straight indicating the well coating of the layers and excellent stacking nature.

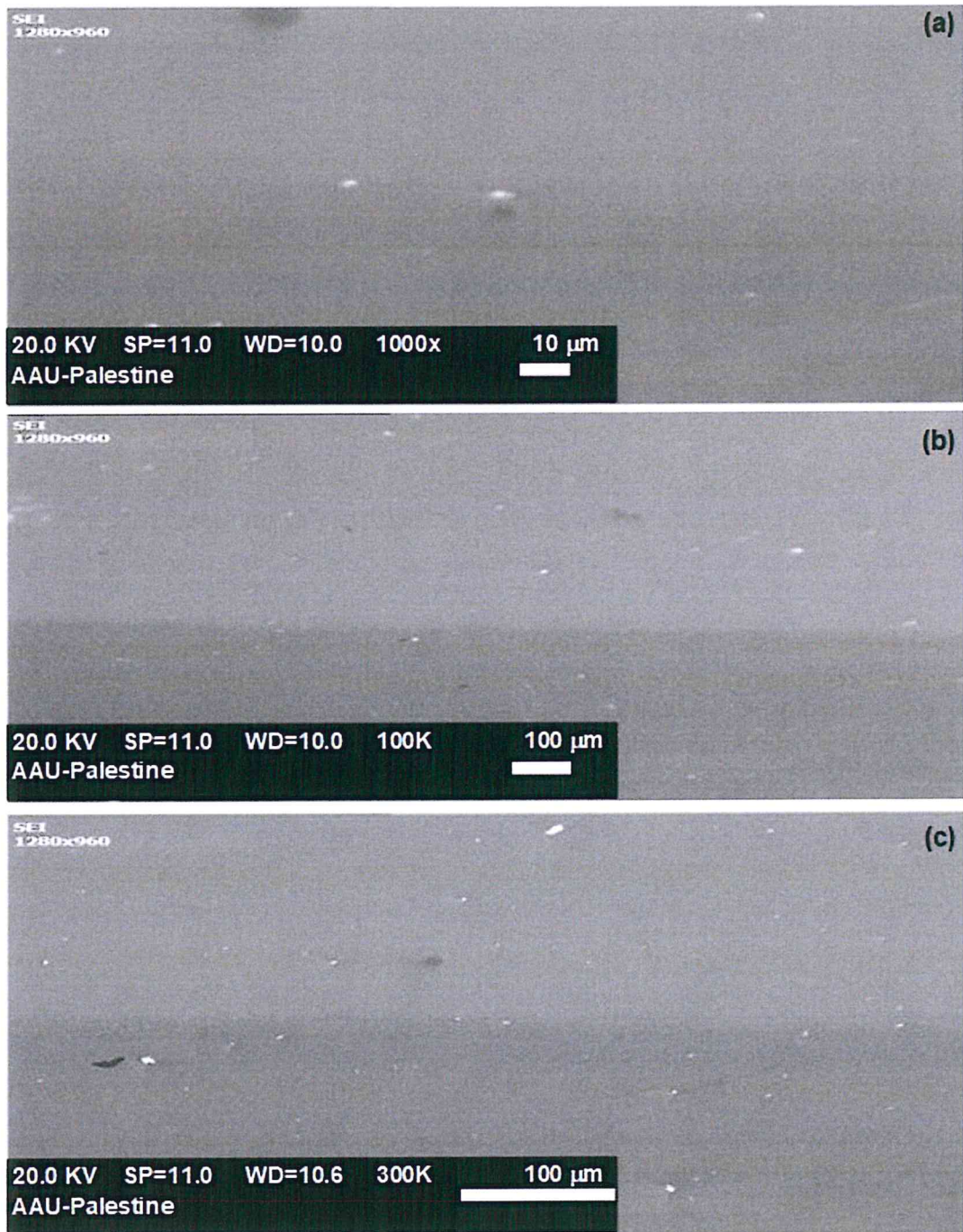


Fig. 4.3: The SEM image for $\text{WO}_3/\text{Ga}_2\text{S}_3$ heterojunction deposited on glass for (a) 1K (b) 100K (c) 300K enlargements.

Three regions were selected to present the energy dispersive X-ray analysis for $\text{WO}_3/\text{Ga}_2\text{S}_3$ heterojunctions. Fig. 4.4 displays the EDX spectra for the three samples that demonstrate the atomic compositions of the studied regions. In Fig. 4.4(a) WO_3 region clearly shows the presence of W and O in the sample. While Fig. 4.4(b) displays the $\text{WO}_3/\text{Ga}_2\text{S}_3$ region which shows W, O, S and Ga atoms in the sample structure with larger percentage of W and O atoms. The Ga_2S_3 region exhibits the same composition of the second region but the maximum percentage is detected for Ga and S atoms as appear in Fig. 4.4(c). The EDX measurements gain importance owing to its ability to emphasize the presence of sulfur atoms which are known to be volatile. It also confirms, the presence of Ga and S atoms indicating the formation of physical compound and no chemical compound take place. In the three region, the presence of Au atom is due to the coating of the surface of the sample for the purpose of preventing electron contaminations. The appearance of larger intensity is assigned to its presence on top surface.

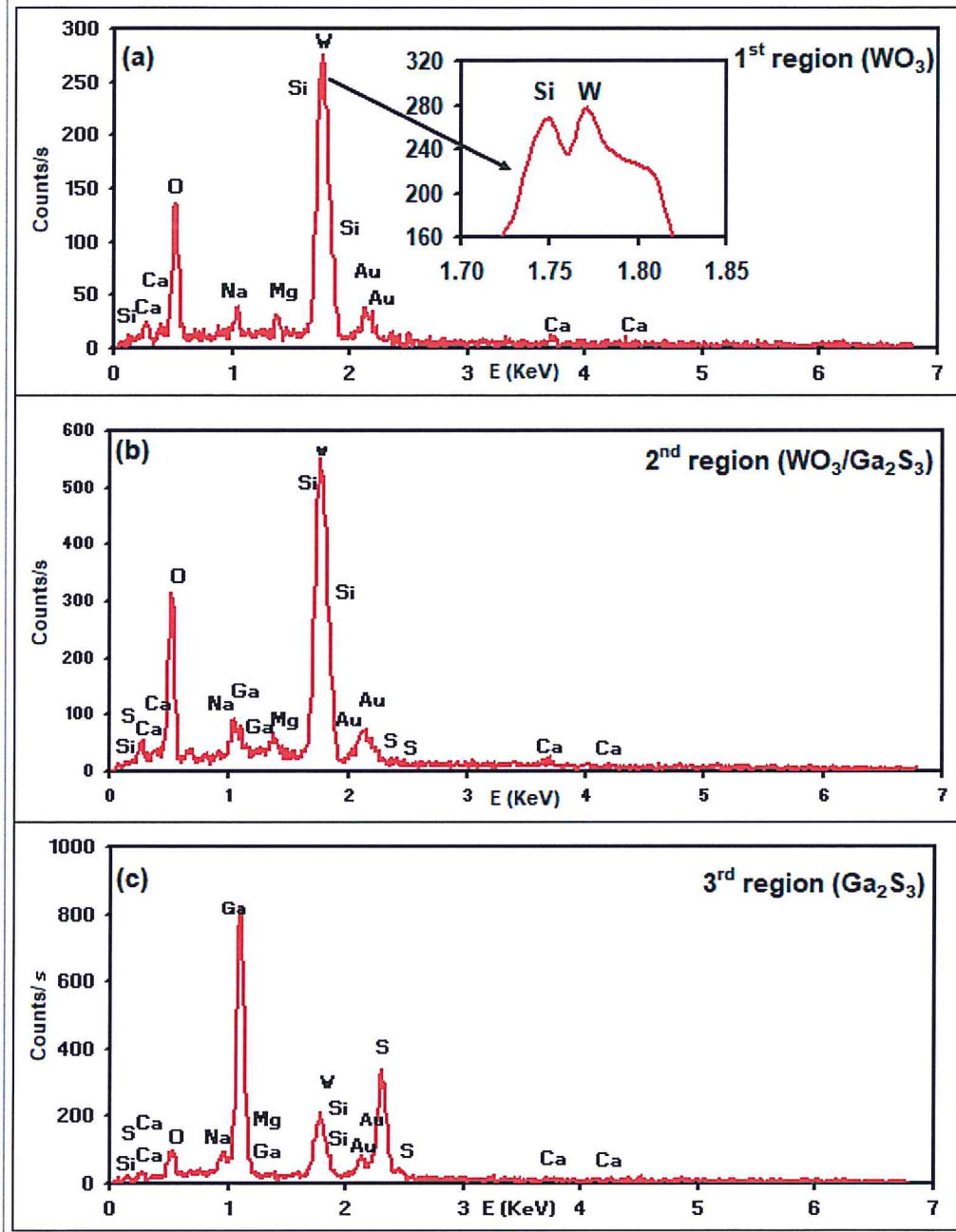


Fig. 4.4: The EDX spectra for (a) WO_3 (b) $\text{WO}_3/\text{Ga}_2\text{S}_3$ (c) Ga_2S_3 films.

4.2 Optical analysis

The optical transmittance and reflectance are measured in the wavelength range of 300-1100 nm with the help of an evolution 300 spectrophotometer. The transmittance spectra for the prepared thin films are displayed in Fig. 4.5.

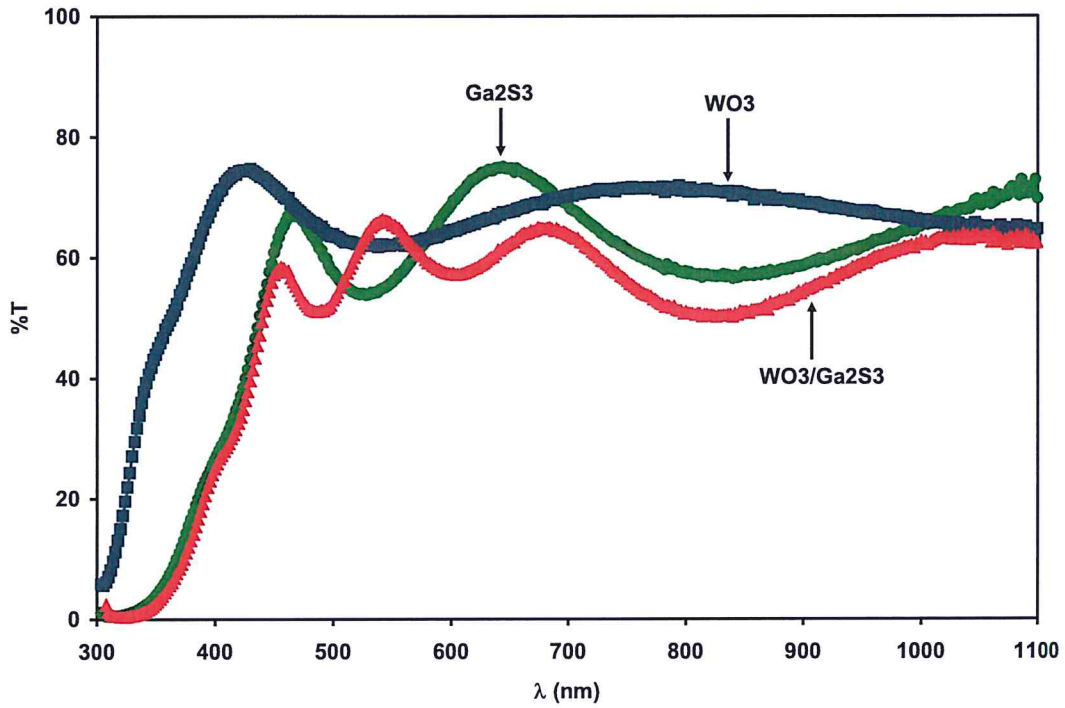


Fig. 4.5: The transmittance spectra for WO₃, Ga₂S₃ and WO₃/Ga₂S₃ thin films on glass substrates.

As can be seen from the above figure, all thin films have high transmittance. For WO₃ one interference peak appears with maximum value of 74.67% at 430 nm. Whereas, Ga₂S₃ thin film shows two interference peaks with maxima of 75.01% at 644 nm. For the WO₃/Ga₂S₃ heterojunctions three interference peaks were observed and the maxima of 66.28% appear at 542 nm. The maxima of the transmittance peaks are also tabulated in table 4.1 for easy comparison. Clearly, these values indicate that the Ga₂S₃ has the

highest transmittance. The transmittance spectra for both Ga_2S_3 and $\text{WO}_3/\text{Ga}_2\text{S}_3$ have approximately similar behavior.

The reflectance spectra for the WO_3 , Ga_2S_3 and $\text{WO}_3/\text{Ga}_2\text{S}_3$ thin films are illustrated in Fig. 4.6.

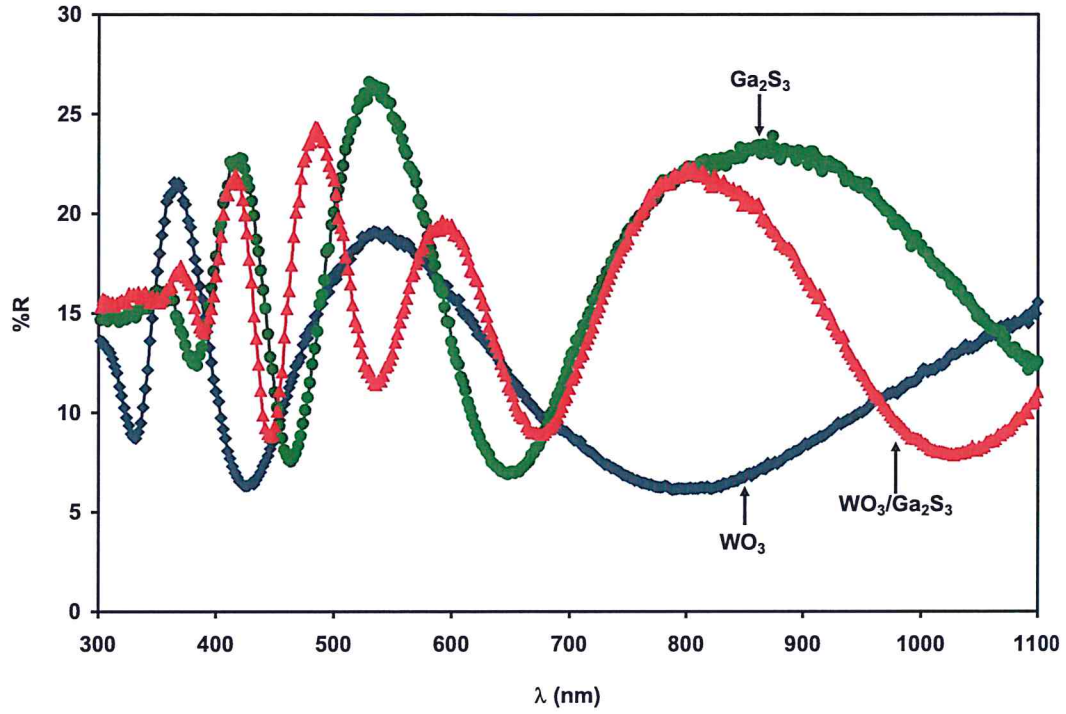


Fig. 4.6: The reflectance for the WO_3 , Ga_2S_3 and $\text{WO}_3/\text{Ga}_2\text{S}_3$ thin films on glass substrates.

As it is obvious from the figure, all thin films have peaks at various values of wavelengths. Two, four and five peaks appeared in WO_3 , Ga_2S_3 and $\text{WO}_3/\text{Ga}_2\text{S}_3$ thin films, respectively. The maximum values of reflectance are 21.56%, 26.59% and 24.34% occur at wavelengths of 364, 530 and 484 nm for WO_3 , Ga_2S_3 and $\text{WO}_3/\text{Ga}_2\text{S}_3$ thin films, respectively. In addition, the reflectance spectra of Ga_2S_3 and $\text{WO}_3/\text{Ga}_2\text{S}_3$ exhibited

approximately the same behavior. Namely, the same location of the observed peaks with slight shifts.

Very interesting features are detected is the absorption coefficient (α) spectra which was calculated with the help of Eqns. (2.11) and (2.13) for single and double layers, respectively. Redefining Eqn. (2.14 as below. The α -spectra are illustrated in Fig. 4.7.

$$\alpha = -\frac{1}{d} \ln\left(\frac{T}{(1-R_{glass})(1-R_{WO_3})(1-R_{WO_3/Ga_2S_3})}\right) \quad (4.1)$$

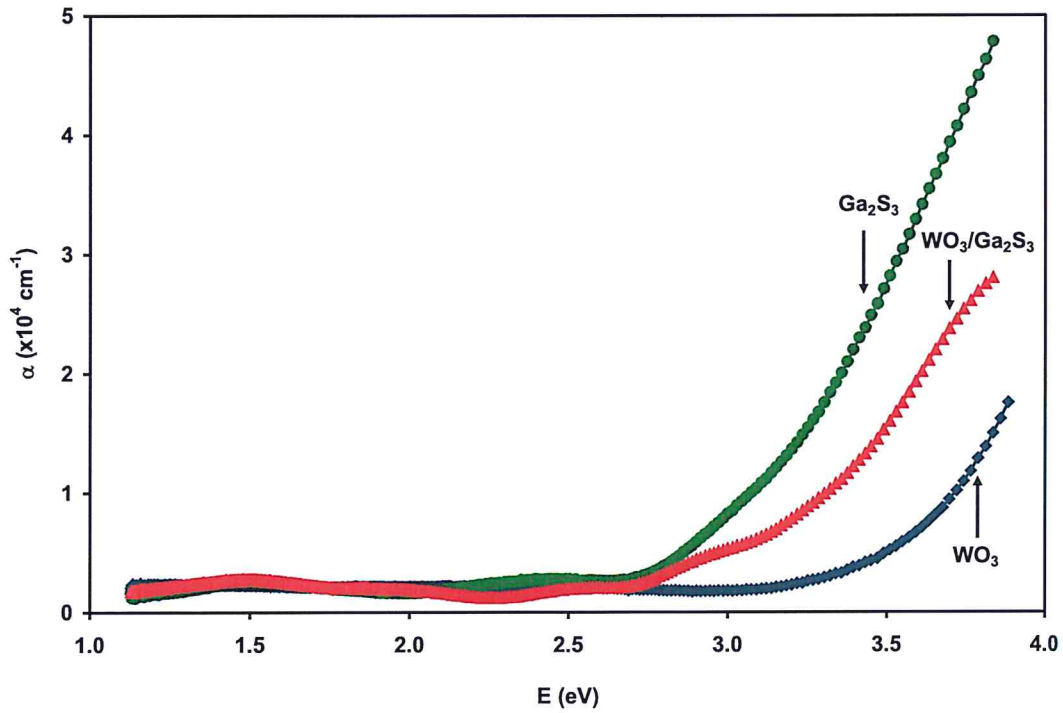


Fig. 4.7: The absorption coefficient (α) for WO_3 , Ga_2S_3 and $\text{WO}_3/\text{Ga}_2\text{S}_3$ thin films.

As clear from Fig. 4.7, the absorption coefficient for Ga_2S_3 is similar to that for $\text{WO}_3/\text{Ga}_2\text{S}_3$ films with some shifts. For both samples, α begins with low absorption coefficient and then starts to increase with increasing incident photon energy for energy

values of 2.68 eV. WO_3 films have nearly constant absorption coefficient in the range between (1.0-3.1 eV) as the light energy exceeds 3.1 eV, α increases sharply with increasing photon energy. The nonzero values of α -spectra for all the films and the decreasing trend of variation for Ga_2S_3 and $\text{WO}_3/\text{Ga}_2\text{S}_3$ are assigned to the formation of interbands through the band gap of WO_3 and Ga_2S_3 . Interbands in WO_3 and Ga_2S_3 may have formed by the presence of sulfur, oxygen, tungsten and gallium vacancies [8]. It is also possible to consider that the formation of Ga_2O_3 at the ultrathin interface could have caused extended energy states that increased the already existing band tails of Ga_2S_3 .

Tale 4.1: The calculated optical measurements for WO_3 , Ga_2S_3 and $\text{WO}_3/\text{Ga}_2\text{S}_3$ thin films.

Thin film	T% max	R% max	E_g (eV)	E_c (eV)
WO_3	74.67	21.56	3.17	0
Ga_2S_3	75.01	26.59	2.53	0.54
$\text{WO}_3/\text{Ga}_2\text{S}_3$	66.28	24.34	2.62	0.78

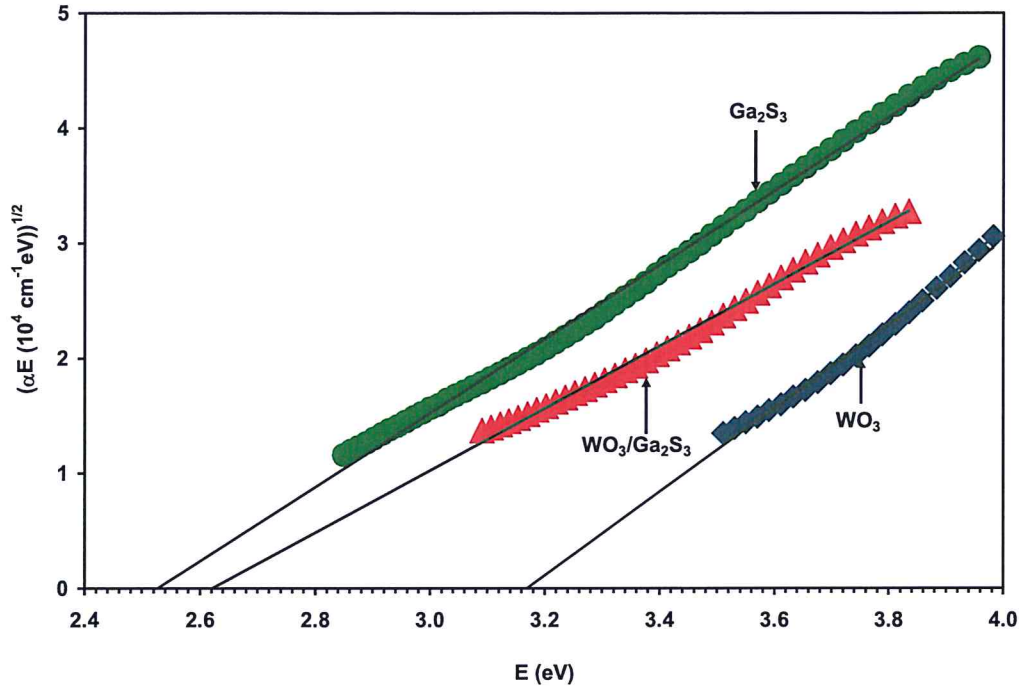


Fig. 4.8: The calculated indirect energy band gaps using Tauc equation fitting for WO_3 , Ga_2S_3 and $\text{WO}_3/\text{Ga}_2\text{S}_3$ thin films.

By using Tauc equation (2.14) and restricting linear fittings, the energy band gaps for the films under investigated were determined. The selected value of p refers to the widest range of linear fitting of the data. It refers to p -value of 2 in our samples. From the intercepts of $(\alpha E)^{1/2}$ - E variations, the energy crossing at 3.17, 2.53 and 2.62 eV for WO_3 , Ga_2S_3 and $\text{WO}_3/\text{Ga}_2\text{S}_3$ are determined, respectively. These values correspond to electronic transitions of indirect allowed type. The literature value of E_g for WO_3 is 3.25 eV [30, 31]. The literature data for monoclinic and hexagonal Ga_2S_3 are 3.44, 2.48 eV, respectively [54]. The determined experimental energy band gap values are closed to the literature data. As can be seen, the energy band gap for WO_3 is large compared to the others. Interfacing Ga_2S_3 with WO_3 gives a moderate band gap between them. In other words, the coating of Ga_2S_3 onto WO_3 shrinks the energy gap. The narrowing of the

energy band gap allows further electronic transitions between the valence and the conduction bands and improves the conductivity of the $\text{WO}_3/\text{Ga}_2\text{S}_3$ interfaces. In comparison to another work, which concern coating Ga_2S_3 over selenium (Se), a direct allowed transition energy band gap is formed with value 1.94 eV [68].

Another important quantity is the interband energy (E_e) which can be determined from the slope of plotting $\ln(\alpha)$ versus Energy. Using Eqn. (2.51), the reciprocal of the slopes which are shown in Fig. 4.8 gives the interband energy widths (E_e). The values of E_e that are shown in Table 4.1 are zero, 0.54 and 0.78 eV for WO_3 , Ga_2S_3 and $\text{WO}_3/\text{Ga}_2\text{S}_3$, respectively. These values indicate that WO_3 thin film has no interbands in the energy gap while the nonzero values of Ga_2S_3 and $\text{WO}_3/\text{Ga}_2\text{S}_3$ are response to the presence of interbands in the band gap of Ga_2S_3 .

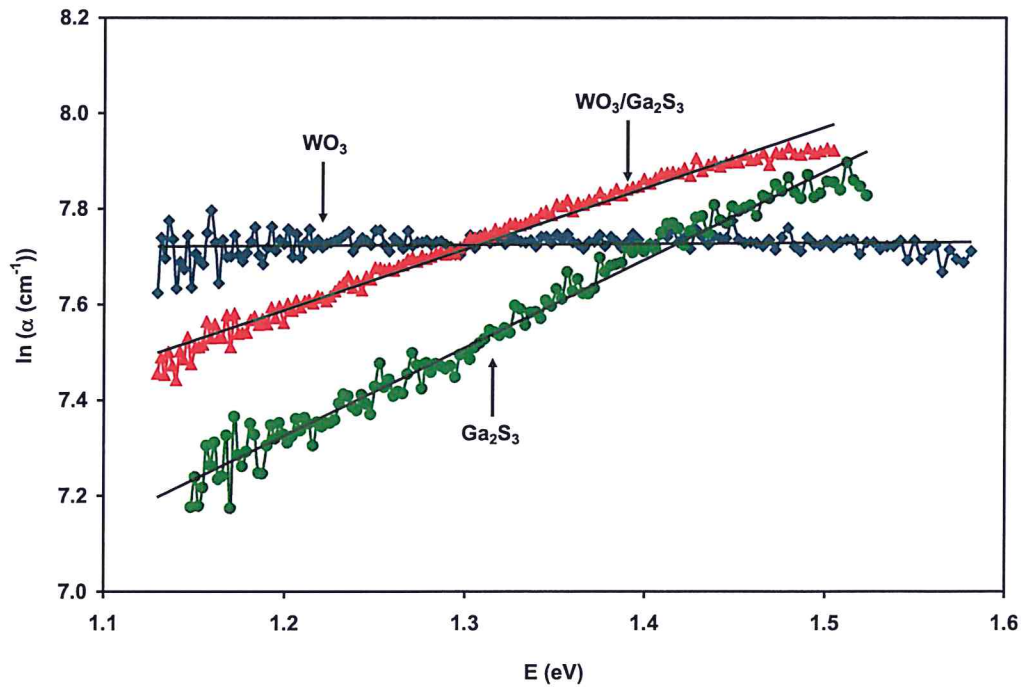


Fig. 4.9: The determined interband energies (E_e) for WO_3 , Ga_2S_3 and $\text{WO}_3/\text{Ga}_2\text{S}_3$ thin films.

The effective dielectric constant (ϵ_{eff}) and the extinction coefficient (K) are also determined with the help of T , R and α spectra data using Eqns. (B.22) and (2.89), respectively. The real part of the dielectric constant (ϵ_r) was calculated from ϵ_{eff} using Eqn. (B.30) and plotted in Fig. 4.10.

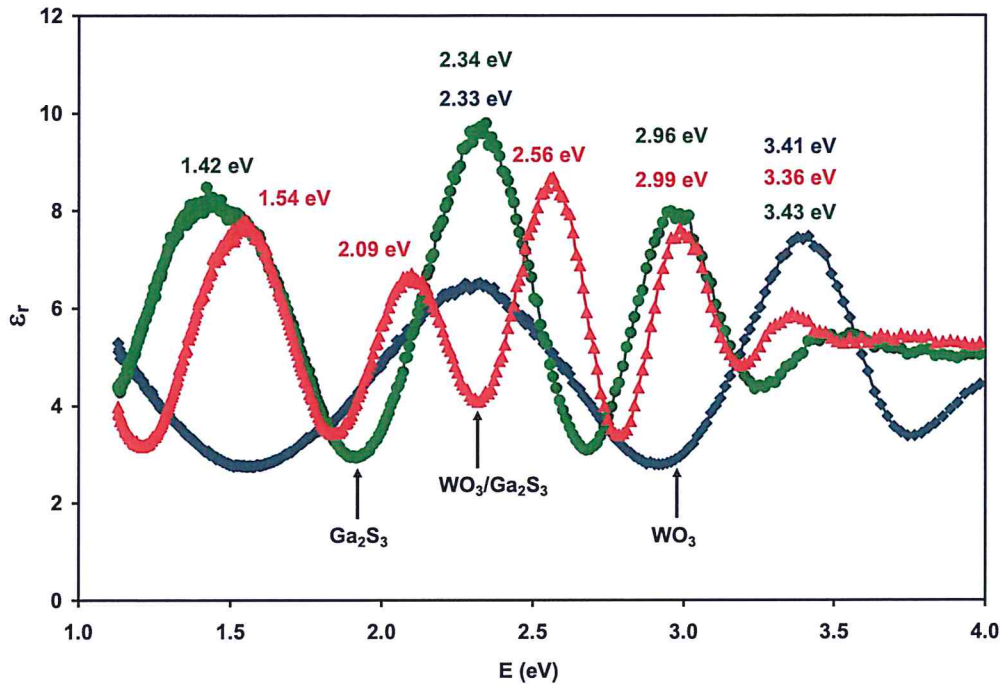


Fig. 4.10: The real part of dielectric constant for WO₃, Ga₂S₃ and WO₃/Ga₂S₃ thin films.

The figure displays the behavior of the real part of dielectric constant for the studied thin films. The dielectric constant spectra follow the same behavior like that of the reflectance spectra. While the spectra of WO₃ displayed only two peaks and the Ga₂S₃ shows four peaks, the WO₃/Ga₂S₃ included five peaks in its spectra. The observed peaks in WO₃ film are centered at 2.33 and 3.41 eV. The value being 3.41 eV is ascribed to the optical band gap of amorphous WO₃ [69]. Whereas, Ga₂S₃ indicates four peaks which are centered at 1.42, 2.34, 2.96 and 3.43 eV. The observed resonance peaks at 2.34 eV and

3.43 eV are mostly assigned to the transitions of β -Ga₂S₃ and α -Ga₂S₃ phases, respectively. In another study, the photonic transition is reported to be through energy band gap of 3.44 and 2.48 eV for α -Ga₂S₃ and β -Ga₂S₃, respectively [22]. Previously, it mentioned that the direct allowed transitions energy band gap of Ga₂S₃ is 2.96 eV [56]. The resonance peak shown at 1.42 eV is attributed to the interband transitions through the energy bands of the Ga₂S₃ thin films. Comparing the previously published works to the current study, a resonance peak was observed at 1.32 eV. This peak is assigned to the interband transitions through the energy band gap of the Ga₂S₃ [56]. As we discussed in the XRD part, the amorphous nature of Ga₂S₃ which was due to the polymorphic phases [55] are also assigned to the surface defects [56]. The films may comprise more than one polyphases in its structure. On the other hand, five peaks appear in the real part of dielectric spectra at energies of 1.54, 2.09, 2.56, 2.99 and 3.36 eV for WO₃/Ga₂S₃ films. The values being 3.36 and 2.56 eV are assigned to the presence of α and β -polymorphic phases in gallium sulfide, respectively. The slight shift in the values are ascribed to the presence of WO₃ which causes strained structure. The energy value at 2.99 eV are also ascribed to the direct allowed transitions energy band gap of Ga₂S₃ [56]. In addition, the resonance peak at 1.54 eV may be assigned to the interband transitions through the energy band gap of Ga₂S₃ [56]. Taking into consideration the chemical reactions that occurred between tungsten oxide and gallium sulfide resulting in formation of Ga₂O₃, the observed peaks are not assigned to these compounds. By comparison to another work, when Ga₂S₃ was deposited onto Al, it exhibits three resonance peaks that correspond to oscillator energies of 3.26, 2.62 and 1.76 eV. The third peak was possibly attributed to the interband transitions through the energy band of Ga₂S₃ films [55].

The imaginary part of dielectric spectra (ϵ_{im}) which is calculated with the help of Eqn. (B.31) are presented in Fig. 4.11. Different style of variation appears in the figure. For WO_3 thin film, the imaginary part is, approximately, constant until the incident photon energy reaches 3.4 eV. It then begins to increase slowly. However, for Ga_2S_3 the dielectric extremely increased as the light energy exceeds 2.7 eV. In contrast to this behavior, $\text{WO}_3/\text{Ga}_2\text{S}_3$ heterojunction nearly display invariant trend with increasing energy.

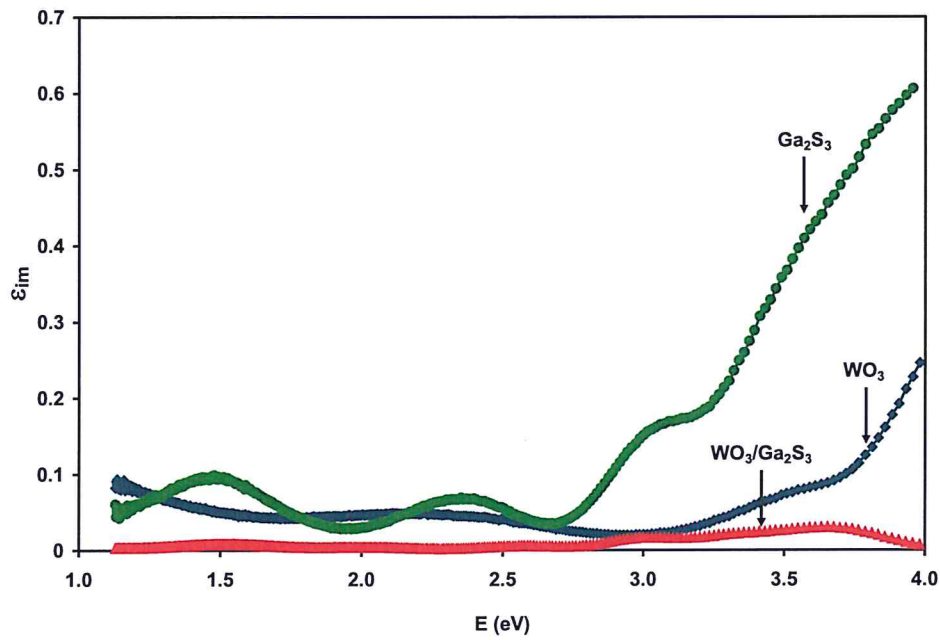


Fig. 4.11: The imaginary part of dielectric constant for WO_3 , Ga_2S_3 and $\text{WO}_3/\text{Ga}_2\text{S}_3$ thin films.

From passive device point of view, the quality factor which is defined as the ratio of the ϵ_r to ϵ_{im} remarkably increases upon $\text{WO}_3/\text{Ga}_2\text{S}_3$ interfering. As for example at 1.5 eV, the quality factor exhibit values of 55.6, 8.22 and 897.6 for WO_3 , Ga_2S_3 and $\text{WO}_3/\text{Ga}_2\text{S}_3$, respectively.

Another important physical parameter which can be obtained from the imaginary part is the optical conductivity. The imaginary part of dielectric and angular frequency of the incident light are employed to calculate the optical conductivity using Eqn. (2.44). The optical conductivity spectra for WO_3 , Ga_2S_3 and $\text{WO}_3/\text{Ga}_2\text{S}_3$ thin film are displayed in Fig. 4.12. Conductivity spectra are similar in behavior of the imaginary part of dielectric due to the direct relationship between them.

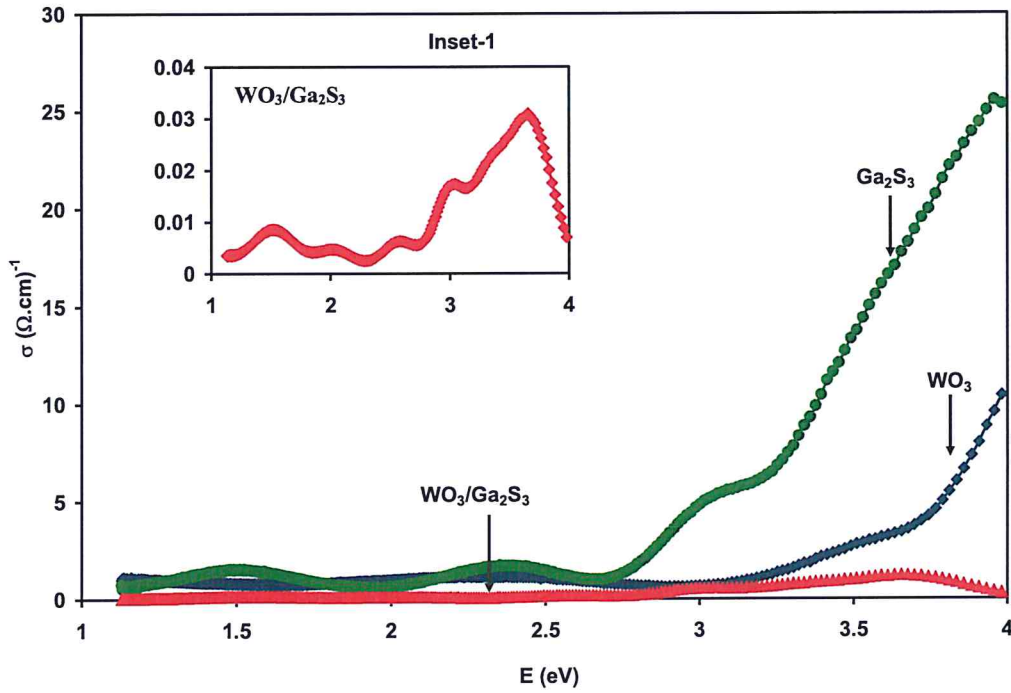


Fig. 4.12: The optical conductivity spectra for WO_3 , Ga_2S_3 and $\text{WO}_3/\text{Ga}_2\text{S}_3$ thin films.

The magnitude of conductivity differs for all films; maximum conductivity is observed for Ga_2S_3 films. Oppositely, the minimum conductivity is detected for $\text{WO}_3/\text{Ga}_2\text{S}_3$ heterojunction. Namely, it is clear from the figure that the deposition of amorphous Ga_2S_3 onto amorphous WO_3 lowers the value of the optical conductivity owing to the increased randomness at the surface. The optical conductivity for the double junction is shown in

the enlargement which appears in inset-1 in Fig. 4.12. The decrease in the value of σ upon $\text{WO}_3/\text{Ga}_2\text{S}_3$ interfacing can be assigned to the increased randomness at the interface owing to the amorphous nature of the two films.

4.3 Electrical properties

4.3.1 Current (I)-Voltage (V) characteristics

When a metal is contacted with a semiconductor, a barrier is formed in the metal-semiconductor interface. This formed barrier controls the current conduction and the capacitance behavior. In the p-n junction the current transport is mainly due to the minority carriers, in contrast to the metal-semiconductor contacts, the majority carriers are responsible of conduction [47]. In the case of metal-semiconductor contact, charge will move from the semiconductor to the metal until thermal equilibrium is established. The I-V characteristics for $\text{Yb}/\text{WO}_3/\text{Au}$ and $\text{Yb}/\text{WO}_3/\text{Ga}_2\text{S}_3/\text{Au}$ interfaces are measured using computerized a Keithley 6485 picoammeter and a Keithley 230 voltage source in the dark. The current behavior of each device is investigated in the following figures that represent the forward and reverse bias in the presence of applied voltage.

From the measured I-V characteristics of $\text{Yb}/\text{WO}_3/\text{Au}$, there is no rectification indicating the ohmic nature of the $\text{Yb}/\text{WO}_3/\text{Au}$ contact. This behavior is not normal as a schottky contact was expected. It most probably happens due to the large defect density at the interface which may form short channels of conduction.

For the heterojunction devices, Fig. 4.13 shows the current-voltage graph for $\text{Yb}/\text{WO}_3/\text{Ga}_2\text{S}_3/\text{Au}$ in the range of -5 to 5 V. It is clear that the rectification of the device increase by adding Ga_2S_3 films, at forward bias the current is $28.4 \mu\text{A}$ at 4 V where at

reverse bias it exhibit value of $-5.18 \mu\text{A}$ at -4 V . The forward current is large compared to the reverse current.

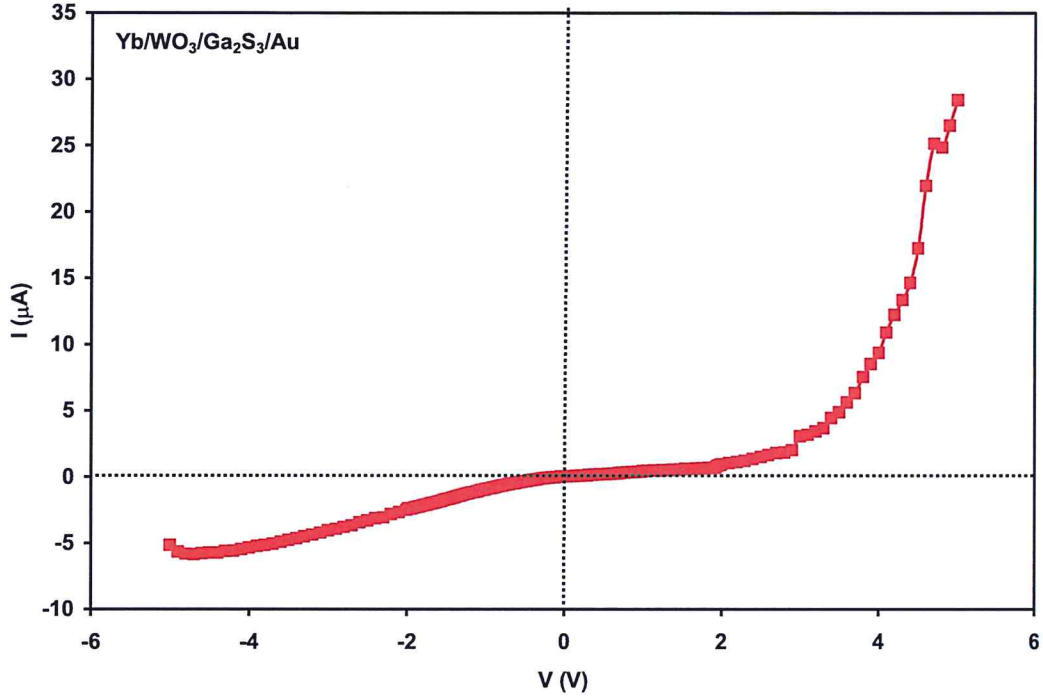


Fig. 4.13: The I-V characteristic for $\text{Yb/WO}_3/\text{Ga}_2\text{S}_3/\text{Au}$ device.

In general, the basic transport processes in the forward process is mainly due to the emission of electrons from the semiconductor over the barrier, diffusion of electrons in the depletion region, injection of holes from the metal to semiconductors, tunneling of electrons through the barrier and recombination process [47]. Assuming the thermionic emission to be mainly responsible for the transport of electrons in $\text{Yb/WO}_3/\text{Ga}_2\text{S}_3/\text{Au}$ devices, we have carried out detailed analysis to explore the nature of conduction.

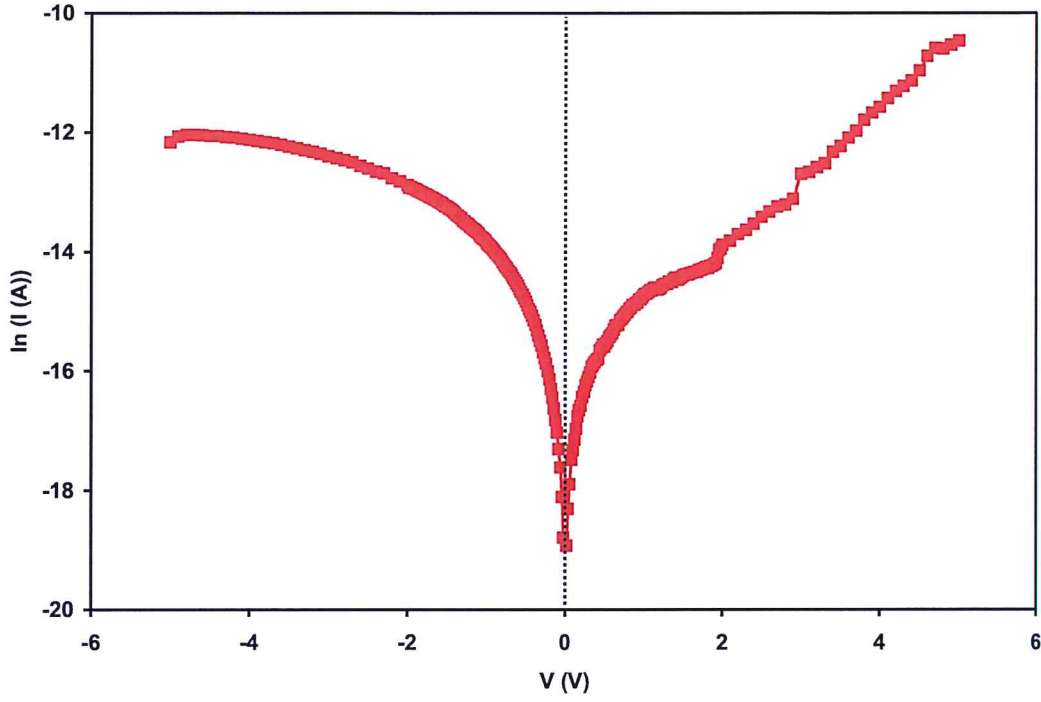


Fig. 4.14: The $\ln(I)$ -V characteristic for Yb/WO₃/Ga₂S₃/Au device.

The figure displays $\ln(I)$ -V variations. Under forward biased conditions, the current increases at the same rate as the reverse at low voltage, but at high voltage the forward current rapidly increases compared to the reverse biased process. The $\ln(I)$ -V analyses were handled assuming thermionic emission of charge carriers over the barrier height. The equation of thermionic emission Eqn. (2.58) was applied substituting the constants as $A = 7.84 \times 10^{-3} \text{ cm}^2$, $A^* = 120 \text{ m}^* = 33.67 \text{ A.cm}^{-2}\text{K}^{-2}$, assuming the effective mass for p-WO₃/n-Ga₂S₃ is $m^* = 0.28 m_0$ which is calculated using

$$\frac{1}{m^*(\text{WO}_3/\text{Ga}_2\text{S}_3)} = \frac{1}{m_h^*(\text{WO}_3)} + \frac{1}{m_e^*(\text{Ga}_2\text{S}_3)} \quad (4.2)$$

Where the hole effective mass for WO₃ (m_h^*) equals $0.94 m_0$ [70] and electron effective mass (m_e^*) for Ga₂S₃ is $0.40 m_0$ [56].

Fig. 4.15 reveals a linearity of $\ln(I)$ in low voltage region, with the ideality factors being 4.46 and 4.96 under forward and reverse bias conditions, respectively. In addition, the forward barrier height was 0.73 eV which is very close to reverse barrier height as 0.72 eV.

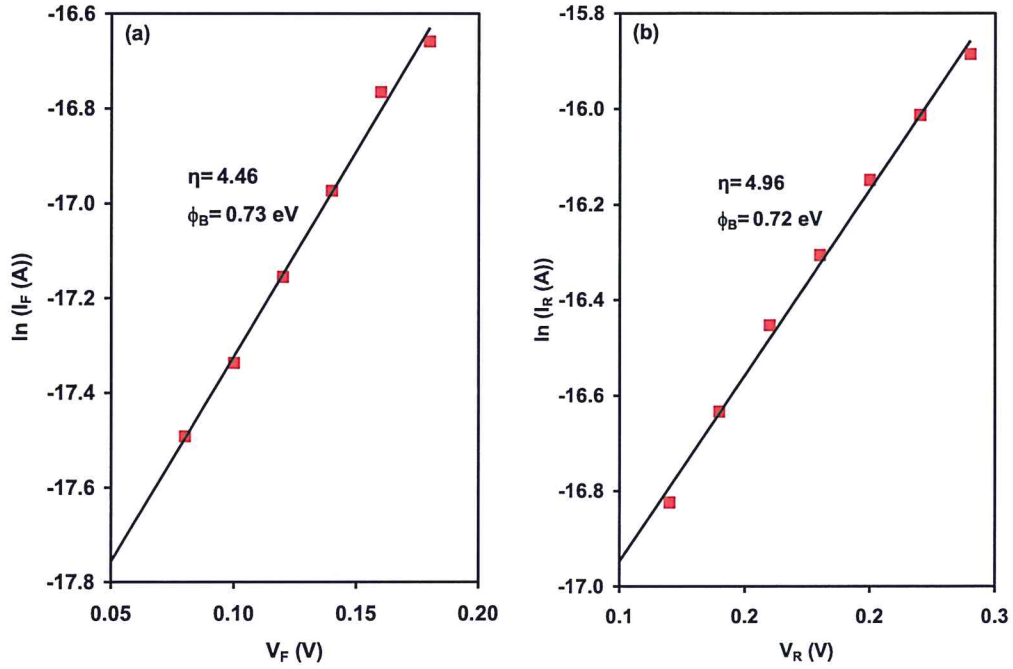


Fig. 4.15: The $\ln(I)$ - V plot at (a) forward and (b) reverse bias for Yb/WO₃/Ga₂S₃/Au device.

The non-unity values of η may be attributed to series resistance effect. To check the series resistance effect, the derivatives $dV/d(\ln(I))$ were evaluated and plotted as a function of I as presented in Fig. 4.16. As seen the derivative gives linear symmetric behavior in low voltage region; using the linear fitting method the slope and intercept are determined. Recalling that the derivative is given by:

$$\frac{dV}{d(\ln I)} = IR_s + \eta \left(\frac{KT}{q} \right) \quad (4.3)$$

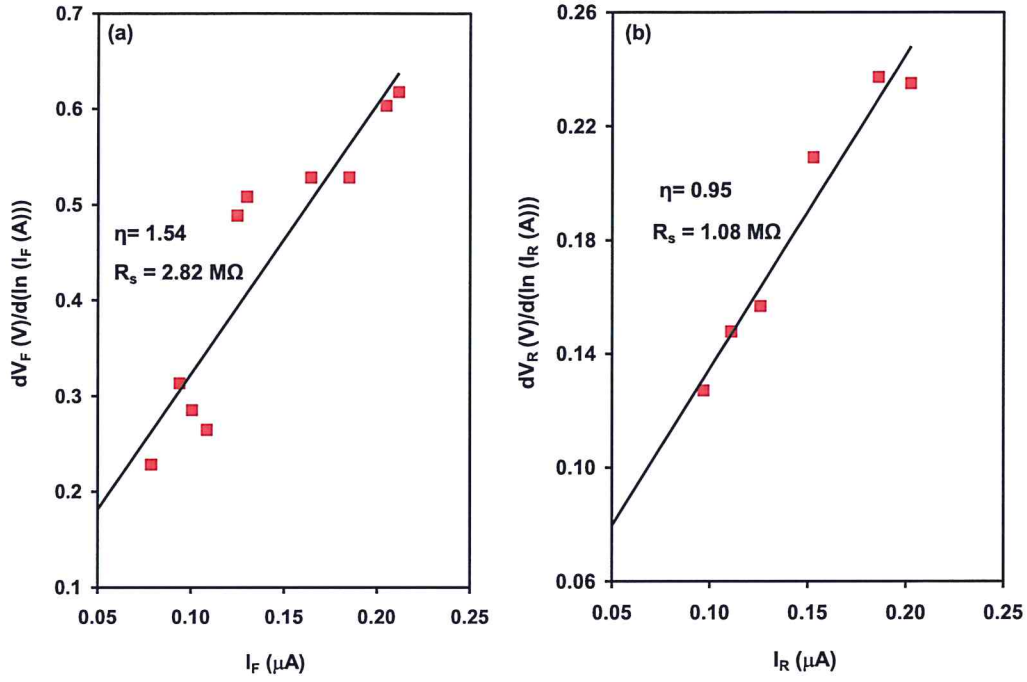


Fig. 4.16: Plot of $dV/d(\ln I)$ versus I at (a) forward (b) reverse bias for Yb/WO₃/Ga₂S₃/Au device. Then, the slope equals the series resistance (R_s) which has large values of 2.82 and 1.08 MΩ at forward and reverse biasing, respectively. While this method reduces the value of η and making it closer to unity, the extrapolation of the graph gives the intercept with the I -axis which indicates the value of η to be equal 1.54 and 0.95 at forward and reverse biasing, respectively, so this method is valid to use Cheung function $H(I)$, which is also based on thermionic emission theory and it is applied to detect the series resistance effect. A plot of Cheung function $H(I)$ from Eqn.(4.4) versus I is displayed in Fig. 4.17, which $H(I)$ can be written as,

$$H(I) = V - \eta \left(\frac{KT}{q} \right) \ln \left(\frac{I}{A A^{**} T^2} \right) \quad (4.4)$$

$$H(I) = IR_s + \eta \phi_B \quad (4.5)$$

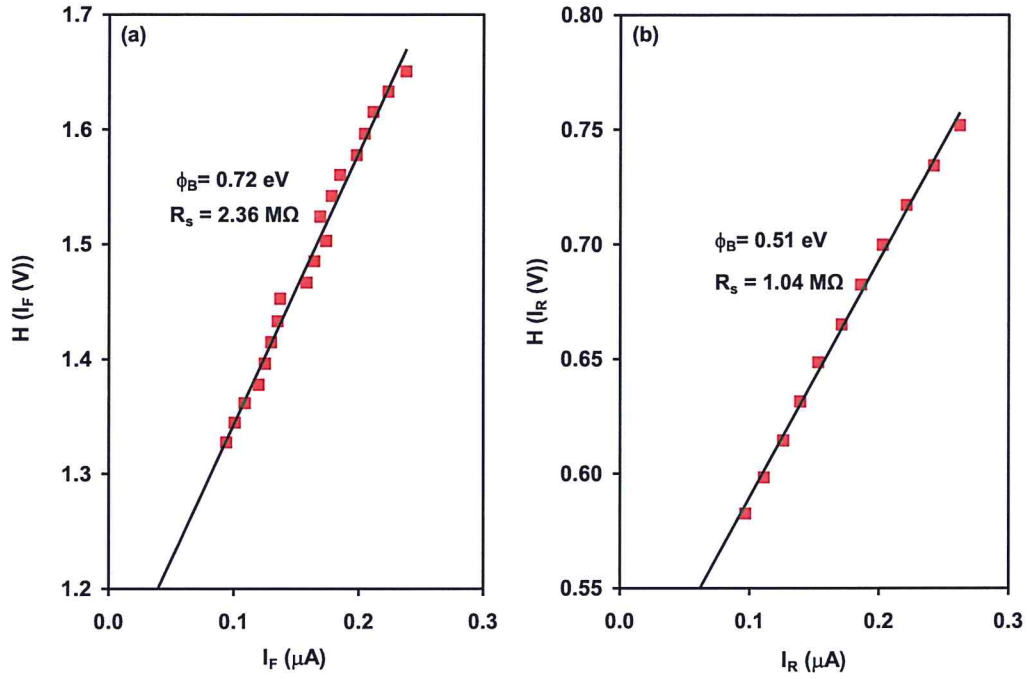


Fig. 4.17: Plot of $H(I)$ versus I at (a) forward and (b) reverse directions for $\text{Yb/WO}_3/\text{Ga}_2\text{S}_3/\text{Au}$ device.

As can be seen from the Fig.4.17, the linearity of the Cheung function as a function of the current helps us find the second determination of series resistance and the barrier height of the device in both directions through Eqn.(4.5). From Fig. 4.17 the slope equals the series resistance which has the value $2.36 \text{ M}\Omega$ and $1.04 \text{ M}\Omega$ for forward and reverse bias, respectively. The values of R_s from figures 16 and 17 are in good agreement with each other. The barrier height which is determined from the slope is found to be 0.72 and 0.51 at forward and reverse process, respectively, as shown in Table 4.2. The values of the barrier height in the forward direction is very close to the values which calculated from Fig.4.15. Whereas in the reverse direction it differs and this may be ascribed to the presence of another current mechanism such as quantum tunneling mechanism.

Table 4.2: The values of R_s , η and ϕ_B using the derivative $dV/d(\ln(I))$ and the Cheung function $H(I)$ for Yb/WO₃/Ga₂S₃/Au schottky devices.

Sample	η	ϕ_B (eV)	R_s (Ω)	η	R_s (Ω)	ϕ_B (eV)
Forward bias	4.46	0.73	2.82 M	1.54	2.36 M	0.72
Reverse bias	4.96	0.72	1.08 M	0.95	1.04 M	0.41

It is not normal to observe that the series resistance and barrier height of the studied samples is larger during the forward bias than the reverse bias. One of the probable reasons of this behavior is the hybrid nature of the device. Namely, the device is composed of p-n junction connected to two back to back schottky diodes. Injection of current from p-side make the p-schottkey forward biased and the majority arrive at the p-side of p-n junction. The junction is also forward biased during this process and as the p-n contacts with minority carriers the other schottky (n-type) is reversed biased so the current is minimized but because the interface resistance between Yb/WO₃ is different than that of Au/Ga₂S₃ are may expect higher values of resistance.

4.4 Energy band diagram

Using the hot-probe technique the conductivity types of semiconductors were identified, WO₃ exhibits p-type, while Ga₂S₃ shows n-type, as a result, anisotype (p-n) heterojunction is formed. The electron affinities and energy band gaps of WO₃ and Ga₂S₃ are $q\chi_1 = 3.33$ eV [71] and $E_g = 3.17$ eV and $q\chi_2 = 3.30$ eV [72] and $E_g = 2.53$ eV, respectively, where the E_g was previously determined from Tauc's equation. The difference in energy gap is $(\Delta E_g = |\Delta E_{g2} - \Delta E_{g1}|) = 0.64$ eV, then, the respective conduction $(\Delta E_c = |q\chi_2 - q\chi_1|)$ and valence band $(\Delta E_v = |\Delta E_g - \Delta E_c|)$ offsets are 0.03 eV and 0.61 eV. As obvious the conduction band offset is approximately zero. In

addition, the work function of WO_3 and Ga_2S_3 are 5.05 eV [73] and 3.46 eV [55], respectively. Because the work function of Yb (2.51 eV) [20] is less than that of WO_3 (p-type), the Yb/ WO_3 interface is schottky contact. Similarly, as the work function of Au (5.34 eV) [74] is larger than that of Ga_2S_3 (n-type), the $\text{Ga}_2\text{S}_3/\text{Au}$ interface forms a schottky barrier. So Yb/ $\text{WO}_3/\text{Ga}_2\text{S}_3/\text{Au}$ reveals hybrid device composed of p-n junction and two Schottky shoulders. The barrier height ($q\phi_B = q\phi_m + E_g - q\chi$) and the built in voltage ($qV_{bi} = q\phi_m + E_g - q\phi_1$) at the Yb/ WO_3 side are 2.35 and 0.63 eV, respectively. The values of ($q\phi_B = q\phi_m - q\chi$) and ($qV_{bi} = q\phi_m - q\phi_1$) for the Au/ Ga_2S_3 are 2.04 and 1.88 eV, respectively. The energy band diagram data of the hybrid device (Yb/ $\text{WO}_3/\text{Ga}_2\text{S}_3/\text{Au}$) reveals good features as electronic device which can be used in telecommunication applications. The deviation of the experimentally calculated barrier height and built in voltage from the theoretically determined most probably ascribed to the surface states which reduces the barrier height through forming short channels for conduction [47].

The energy band diagram for Yb/ $\text{WO}_3/\text{Ga}_2\text{S}_3/\text{Au}$ device is shown in Fig. 4.18.

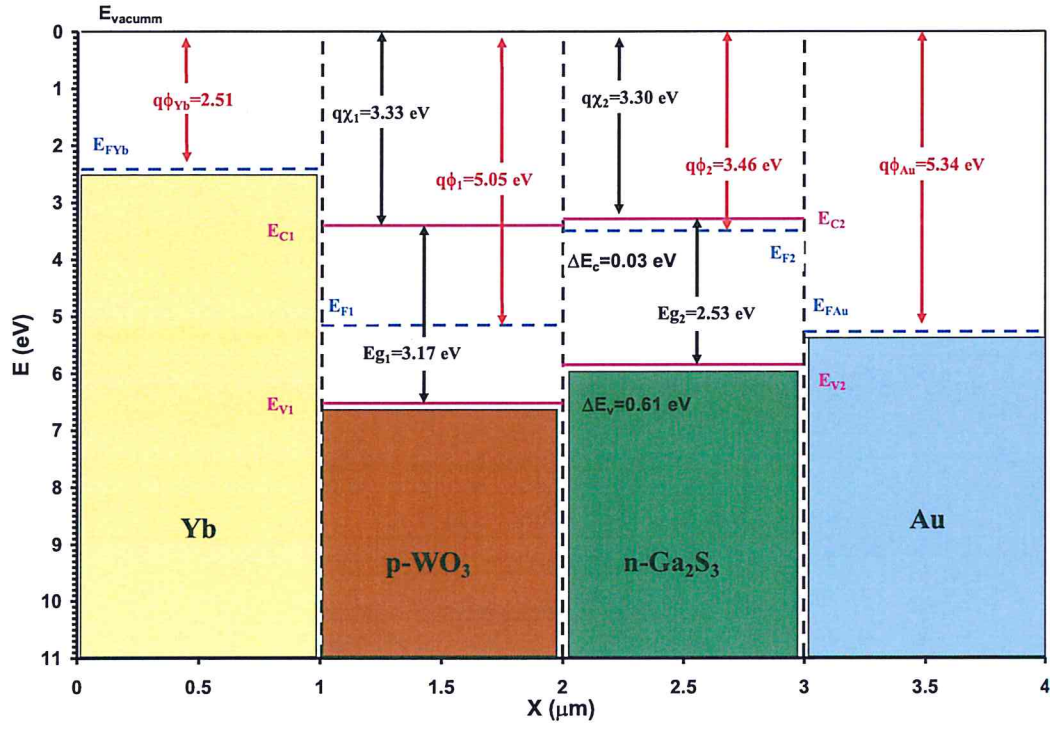


Fig. 4.18: The energy band diagram for Yb/WO₃/Ga₂S₃/Au device.

4.4 The Capacitance (C)-Voltage (V) analysis

The capacitance (C)-voltage (V) characteristics for the Yb/WO₃/Ga₂S₃/Au device which were recorded at low frequency of 1.0 MHz in the voltage range -2 and 2 V are shown in Figure 4.19.

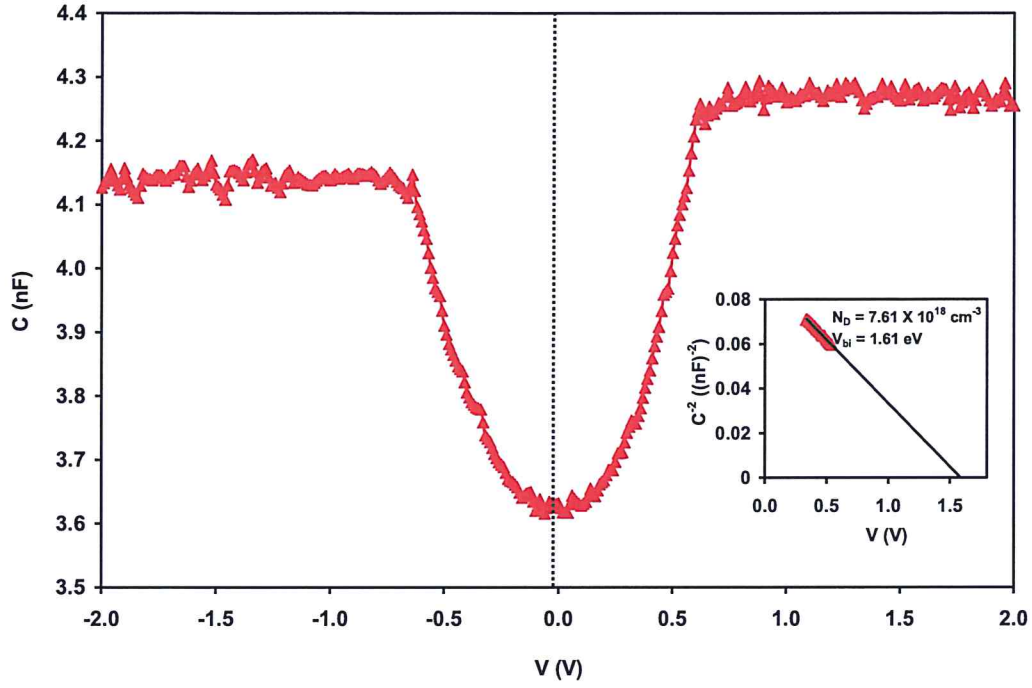


Fig. 4.19: The Capacitance-Voltage characteristic, inset-1 shows the $C^{-2} - V$ variations for Yb/WO₃/Ga₂S₃/Au device.

This figure presents metal-oxide semiconductor MOSFET characteristic in which the device is swept from the accumulation to the inversion mode while measuring the capacitance. At different frequencies in the range of 1-5 MHz, the same behavior was observed. The depletion region of Yb/ WO₃/Ga₂S₃/Au is dominant in the range of 0.62 to -0.65 V depending on the biasing direction. This behavior is similar to that observed for Au/In₄Se₃/Ga₂S₃/C device with a depletion region being dominant in the range of 0.68 to -0.62 V [17]. Plotting $C^{-2}-V$ curve allow determining the built in voltage and effective carrier density through using the relation,

$$C^{-2} = 2(V_{bi} - V - kT/q) / (A^2 q \epsilon N_d) \quad (4.6)$$

The linear behavior was observed in inset-1, the slope of the solid line is used to determine the donor density which is calculated as $7.61 \times 10^{18} \text{ cm}^{-3}$. Whereas, the built in voltage of our hybrid device is also evaluated from the intercept to be equal 1.61 eV.

4.5 Impedance Spectroscopy Analysis

The impedance spectroscopy was investigated in the range of frequency 10-1800 MHz using Agilent 4291B RF Signal Generator impedance analyzer, in which the effect of the AC signal on the samples is studied. In this part, the capacitance, impedance and conductance are investigated as a function of frequency for Yb/WO₃/Au and Yb/WO₃/Ga₂S₃/Au devices.

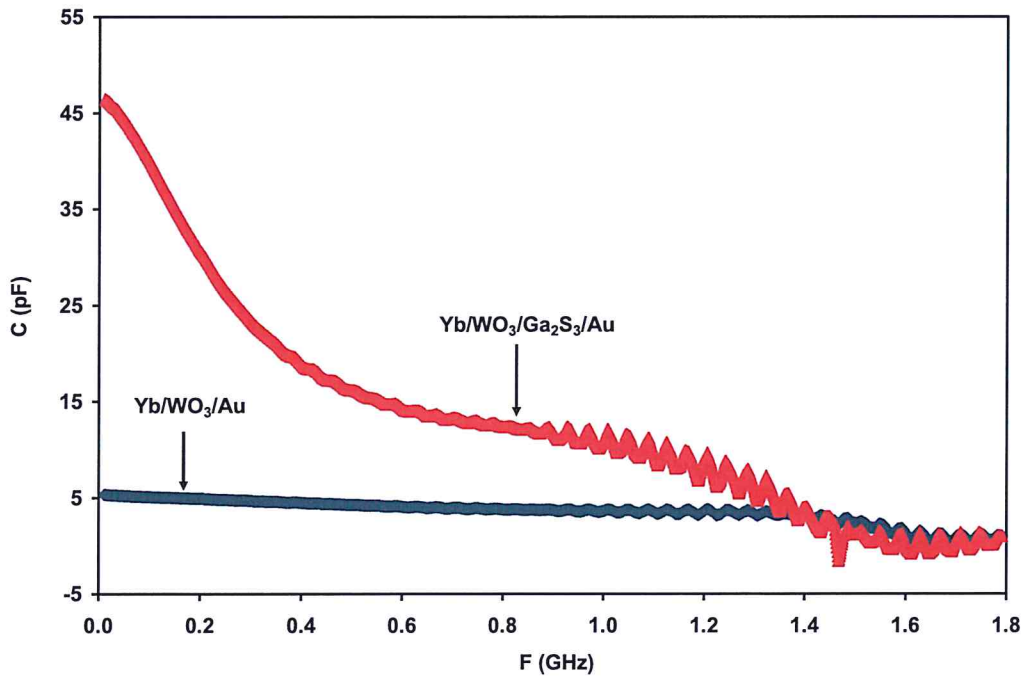


Fig. 4.20: The parallel capacitance for Yb/WO₃/Au and Yb/WO₃/Ga₂S₃/Au devices.

As can see from the figure, the capacitance of $\text{Yb}/\text{WO}_3/\text{Ga}_2\text{S}_3/\text{Au}$ is much larger than that of $\text{Yb}/\text{WO}_3/\text{Au}$. It begins from almost 47 pF then decreases with increasing the frequency to reach 6 pF, while $\text{Yb}/\text{WO}_3/\text{Au}$ exhibits invariant capacitance. These large capacitance values are due to coating of Ga_2S_3 on the surface of WO_3 which forms depletion layer at the interface between Ga_2S_3 and WO_3 .

The impedance (Z) and conductance (G) spectra are shown in Fig. 4.21 and Fig. 4.22, respectively. As shown in Fig.21 the logarithmic plot of impedance versus frequency shows smaller values for $\text{Yb}/\text{WO}_3/\text{Ga}_2\text{S}_3/\text{Au}$ device compared to the $\text{Yb}/\text{WO}_3/\text{Au}$. It is clear that the impedance for $\text{Yb}/\text{WO}_3/\text{Ga}_2\text{S}_3/\text{Au}$ device decreases until the oscillatory field frequency reaches 1.45 GHz. Then after this frequency it starts to increase smoothly in the range 1.45-1.80 GHz. Coating Ga_2S_3 onto WO_3 affected the impedance value, such behavior may be attributed to changes in the current mechanism [75].

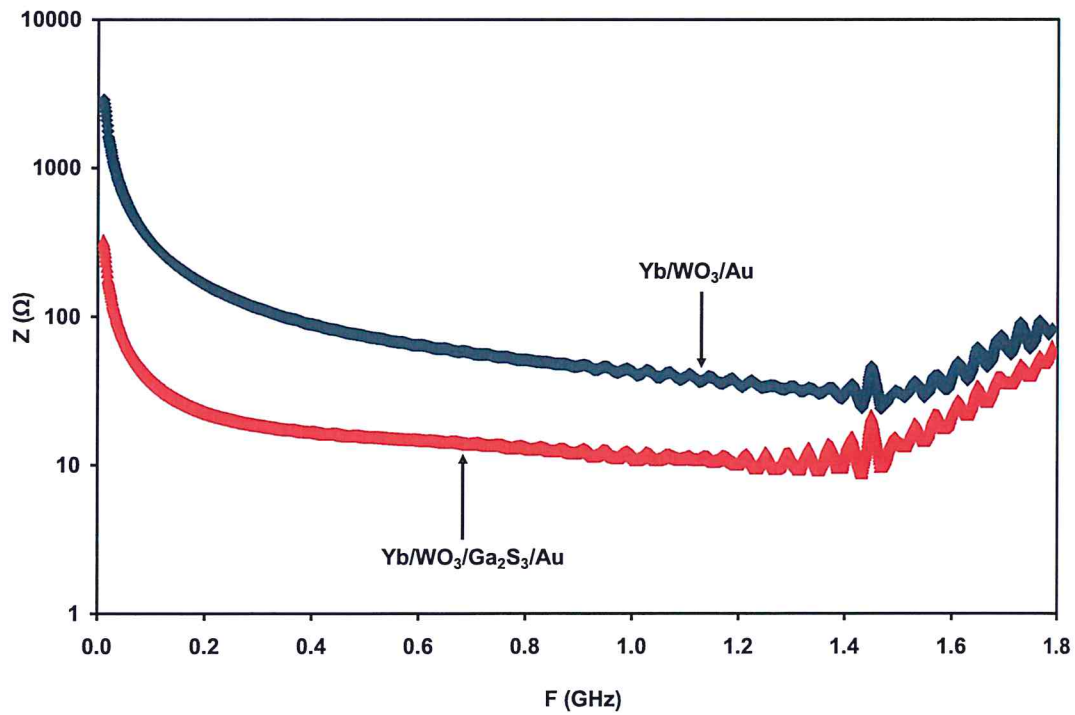


Fig. 4.21: The impedance for $\text{Yb}/\text{WO}_3/\text{Au}$ and $\text{Yb}/\text{WO}_3/\text{Ga}_2\text{S}_3/\text{Au}$ devices.

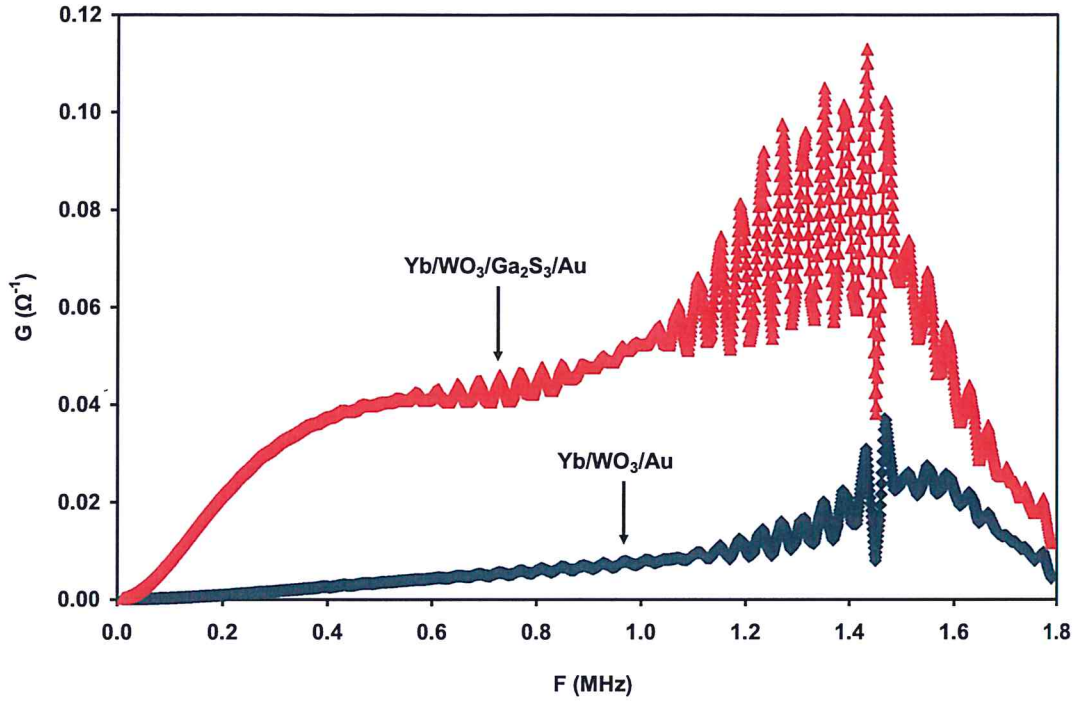


Fig. 4.22: The conductance for Yb/WO₃/Au and Yb/WO₃/Ga₂S₃/Au devices.

In contrast to the behavior of impedance, the conductance (G) increases after depositing Ga₂S₃ onto WO₃ because of the formation of depletion layer at the interface as we mentioned in the capacitance analysis. The trend of variation of the conductance also changes. When the applied signal frequency reaches 1.45 GHz, a maximum in the conductance value is observed. This behavior may be assigned to the current transport mechanism as a result of the surface charge dynamics [75, 76]. It is reported that the increase of conductance with increasing signal frequency happens as a result of quantum mechanical tunneling effect through thin energy barriers. On the other hand, the decreasing trend of variation of conductance with increasing frequency is ascribed to the hopping of charged particles through correlated barriers.

As a complementary work, Fig. 4.23 shows the amplitude of the reflection coefficient (ρ) spectra. The ρ spectra are always less than 1.0, indicating the impedance match between

the device and the source [77]. The better match between the source and the device when ρ has smaller values. Yb/WO₃/Au device exhibits a notch frequency at 1.65 GHz indicating band stop filter features. At this notch frequency (1.65 GHz) the microwave signals are trapped [78]. Similar to the previously mentioned Au/Ga₂S₃/Yb varactor diode can be used as a low/high pass filter or as band stop filter which can be employed in microwave applications [9]. While Yb/WO₃/Ga₂S₃/Au device shows decreasing trend of variation indicating low pass filtering property.

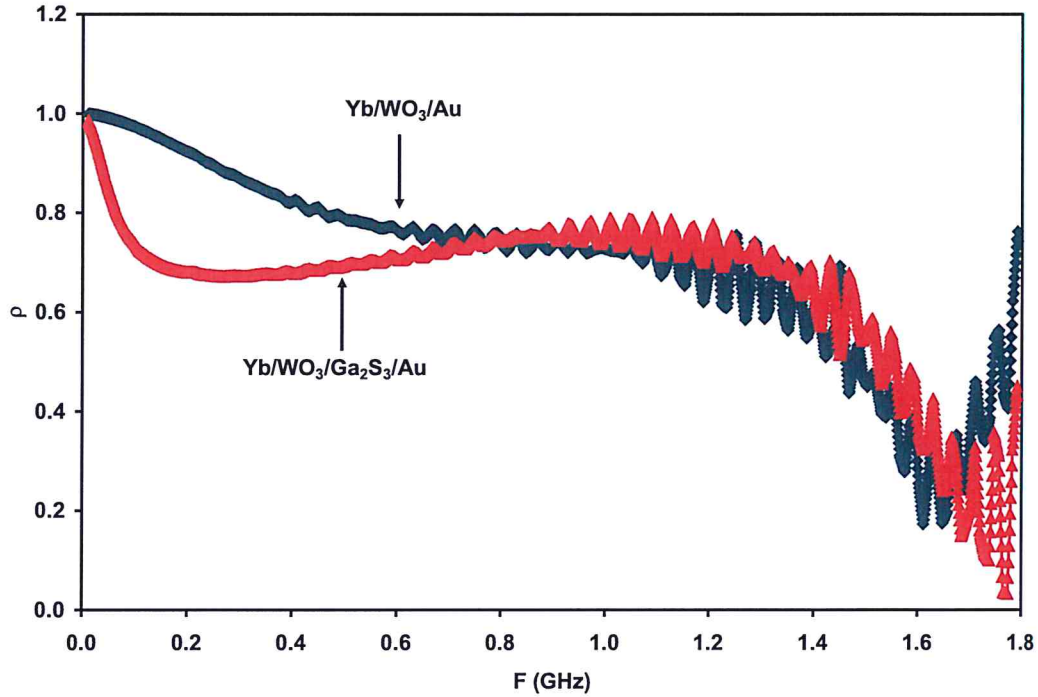


Fig. 4.23: The reflection coefficient(ρ) for Yb/WO₃/Au and Yb/WO₃/Ga₂S₃/Au devices.

The quality of the filters is realized by calculating the absolute value of the return loss as shown in Fig.4.24. We can obtain information about good match for higher values of L_r , the larger value of $L_r \geq |20|$ dB, the better match implied [9]. The maximum L_r value for

Yb/WO₃/Au device is 15.24 dB which is detected at 1.61 GHz. While coating WO₃ with Ga₂S₃ increases L_r to 29.75 dB at frequency of 1.77 GHz. In the light of these numerical analyses, formation of Yb/WO₃/Ga₂S₃/Au heterojunctions highly improved the features of the device as microwave cavity.

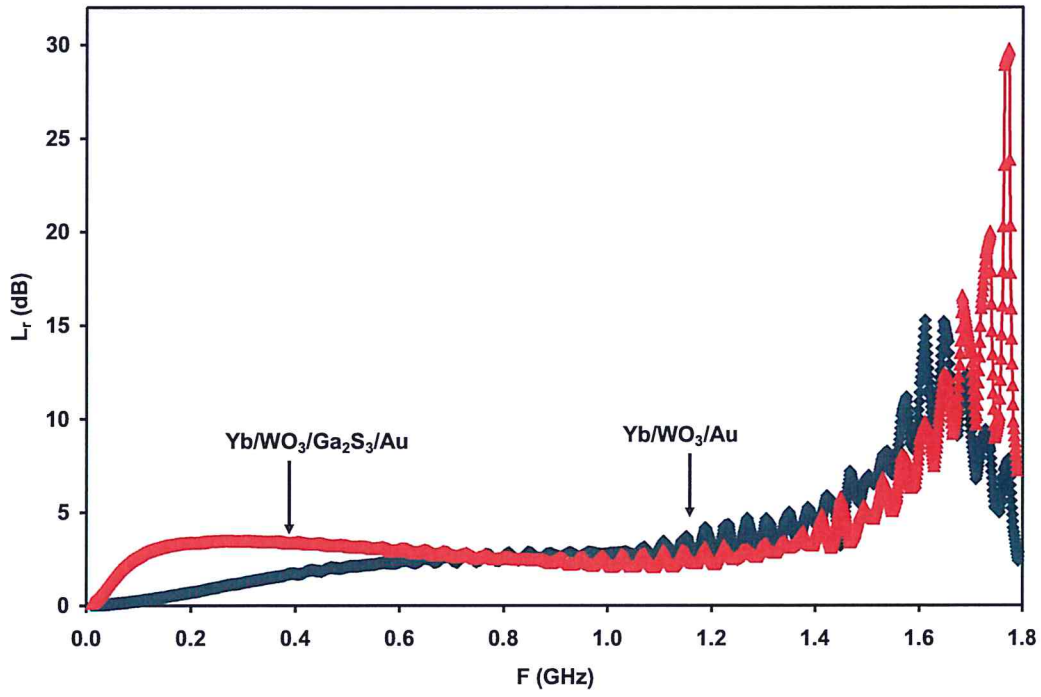


Fig.4.24: The return loss (L_r) for Yb/WO₃/Au and Yb/WO₃/Ga₂S₃/Au devices.

Chapter five

Conclusions

In this we have designed a hybrid device made of WO_3 coated onto Yb thin film substrates and covered with Ga_2S_3 thin film layers. The top contact of the device is made of gold pads. The structural and morphological analysis of the formed structures indicated the formation of physical layers. The heterojunction forms of this device which is prepared onto glass substrates displayed nonlinear optical properties that nominate it for use in optoelectronics. The optical absorption spectral analyses of these two interfaces suggested well aligned conduction bands and valance band offsets that are large enough to make the heterojunction device suitable for the process of quantum confinement needed for separation of electron-hole pairs. The absorbability of WO_3 increased when it was coated with Ga_2S_3 . In addition, the studies of the dielectric spectra of the heterojunction devices displayed different resonance peaks in the visible and IR range of light indicating the usability of the heterojunction to store electromagnetic energy. This property is important when $\text{WO}_3/\text{Ga}_2\text{S}_3$ are used as receivers in visible light communication systems. The electrical characterization presented by the dynamic and passive modes of operation has shown that the device is a rectifier and exhibit features of metal-oxide-semiconductor field effect transistor that can be used for memory storage and as electronic switches. Moreover, the impedance spectroscopy analysis revealed features of tunable capacitor that works at the gigahertz range of frequency. The wide range of impedance variation allowed the device to work at high and low impedance modes. The analysis of the magnitude of the reflection coefficient and return loss spectra

displayed the features of band stop filters nominating the device to be used as microwave cavities.

References

- [1] K. M. Karuppasamy, & A. Subrahmanyam, (2008). The electrochromic and photocatalytic properties of electron beam evaporated vanadium-doped tungsten oxide thin films. *Solar Energy Materials and Solar Cells*, 92(11), 1322-1326.
- [2] M. C. Rao, (2013). Structure and properties of WO₃ thin films for electrochromic device application. *J. Non-Oxide Glasses*, 5, 1-8.
- [3] L. Cheng, X. Zhang, B. Liu, H. Wang, Y. Li, Y. Huang, & Z. Du, (2005). Template synthesis and characterization of WO₃/TiO₂ composite nanotubes. *Nanotechnology*, 16(8), 1341.
- [4] L. Ying-Tao, L. Shi-Bing, L. Hang-Bing, L. Qi, W. Qin, W. Yan, ... & L. Ming, (2011). Investigation of resistive switching behaviours in WO₃-based RRAM devices. *Chinese Physics B*, 20(1), 017305.
- [5] J. Su, L. Guo, N. Bao, & C. A. Grimes, (2011). Nanostructured WO₃/BiVO₄ heterojunction films for efficient photoelectrochemical water splitting. *Nano letters*, 11(5), 1928-1933.
- [6] Z. Huang, J. G. Huang, K. A. Kokh, V. A. Svetlichnyi, A. V. Shabalina, Y. M. Andreev, & G. V. Lanski, (2015). Ga₂S₃: Optical properties and perspectives for THz applications. In *2015 40th International Conference on Infrared, Millimeter, and Terahertz waves (IRMMW-THz)* (pp. 1-2). IEEE.
- [7] H.F. Liu, K.K. Ansah Antwi, N.L. Yakovlev, H.R. Tan, L.T. Ong, S.J. Chua, D.Z. Chi, (2014). Synthesis and phase evolutions in layered structure of Ga₂S₃ semiconductor thin films on epitaxially grown GaAs (111) substrates, *ACS Appl. Mater. Interfaces* 6 3501e3507.
- [8] S. E. Al Garni, & A. F. Qasrawi, (2017). Design and Characterization of the Ge/Ga₂S₃ Heterojunction. *Journal of Electronic Materials*, 46(8), 4848-4856.
- [9] S. E. Al Garni, & A. F. Qasrawi, (2017). Tunable Au/Ga₂S₃/Yb varactor diodes designed for high frequency applications. *Chalcogenide Letters*, 14(9).
- [10] K. V. Madhuri, & M. B. Babu, (2018). Influence of substrate temperature on growth and Electrochromic properties of WO₃ thin films. *Optik*, 174, 470-480.
- [11] Y. N. Liu, M. C. Li, Z. X. Wang, R. Wang H. N. Cui, & S. Q. Xi, (2017). The Preparation and Electrochromic Property of WO₃ Thin Films by Radio Frequency (RF) Magnetron Sputtering. *Mechanics and Materials Science: Proceedings of the 2016 International Conference on Mechanics and Materials Science (MMS2016)* (p. 391).
- [12] M. Yamashita, H. Yamanaka, & H. Wakabayashi, (1996). Thin-film preparation of the Li₂S-GeS₂-Ga₂S₃ glass system by sputtering. *Solid State Ionics*, 89(3-4), 299-304.

- [13] N. Zhou, L. Gan, R. Yang, F. Wang, L. Li, Y. Chen, ... & T. Zhai, (2019). Non-Layered Two-Dimensional Defective Semiconductor γ -Ga₂S₃ toward Broadband Photodetection. *ACS nano*.
- [14] M. Yano, K. Koike, M. Matsuo, T. Murayama, Y. Harada, & K. Inaba, (2016). Growth and crystallographic characterization of molecular beam epitaxial WO₃ and MoO₃/WO₃ thin films on sapphire substrates. *Applied Surface Science*, 381, 32-35.
- [15] A. Tverjanovich, A. Kotikova, & E. N. Borisov, (2007). Photobleaching of Ga₂S₃-GeS₂ films prepared with pulsed laser deposition. *Laser Physics Letters*, 4(5), 341.
- [16] A. Arfaoui, S. Touihri, A. Mhamdi, A. Labidi, & T. Manoubi, (2015). Structural, morphological, gas sensing and photocatalytic characterization of MoO₃ and WO₃ thin films prepared by the thermal vacuum evaporation technique. *Applied Surface Science*, 357, 1089-1096.
- [17] N. M. Khusayfan, A. F. Qasrawi, & H. K. Khanfar, (2018). Design and characterization of Au/In₄Se₃/Ga₂S₃/C field effect transistors. *Results in physics*, 8, 1239-1244.
- [18] D. W. Bullett, (1983). Bulk and surface electron states in WO₃ and tungsten bronzes. *Journal of Physics C: Solid State Physics*, 16(11), 2197.
- [19] R. O. L. A. N. D. Diehl, G. Brandt, & E. K. H. A. R. D. Salje, (1978). The crystal structure of triclinic WO₃. *Acta Crystallographica Section B: Structural Crystallography and Crystal Chemistry*, 34(4), 1105-1111.
- [20] Y. Zhu, X. Zhang, Y. Ji, Y. Feng, & J. Zhang, (2013). Fabrication of WS₂ Nanofibers from WO₃ Nanofibers Prepared by an Electrospinning Method. *Journal of nanoscience and nanotechnology*, 13(3), 1983-1987.
- [21] G. A. De Wijs, P. K. De Boer, R. A. De Groot, & G. Kresse, (1999). Anomalous behavior of the semiconducting gap in WO₃ from first-principles calculations. *Physical Review B*, 59(4), 2684.
- [22] O. Madelung, (2012) Semiconductors: data Handbook. Springer Science & Business Media. Berlin. Doi: 10.1007/978-642-18865-7.
- [23] I. Caraman, D. Rusu, E. Ardeleanu, & I. Evtodiev, (2015). The detectors of uv and x radiation based on Ga₂S₃ and gase semiconductors intercalated with Cd. *Journal of Optoelectronics and Biomedical Materials*, 7(1), 27-32.
- [24] M. Han, X. Zhang, & Z. Zeng, (2014). The investigation of transition metal doped CuGaS₂ for promising intermediate band materials. *RSC Advances*, 4(107), 62380-62386.

- [25] A. F. Qasrawi, (2018). Investigation of the structural and optoelectronic properties of the Se/Ga₂S₃ heterojunctions. *Journal of Alloys and Compounds*, 769, 78-82.
- [26] M. Gillet, C. Lemire, E. Gillet, & K. Aguir (2003). The role of surface oxygen vacancies upon WO₃ conductivity. *Surface Science*, 532, 519-525.
- [27] K. R. Locherer, I. P. Swainson & E. K. H. Salje (1999). Transition to a new tetragonal phase of WO₃: crystal structure and distortion parameters. *Journal of Physics: Condensed Matter*, 11(21), 4143.
- [28] N. M. Khusayfan & H. K. Khanfar, (2018). Optoelectronic properties of the InSe/Ga₂S₃ interfaces. *Results in Physics*, 10, 332-338.
- [29] M. Regragui, V. Jousseume, M. Addou, A. Outzourhit, J. C. Bernede, & B. El Idrissi (2001). Electrical and optical properties of WO₃ thin films. *Thin Solid Films*, 397(1-2), 238-243.
- [30] B. Yagoubi, & C. A. Hogarth (1993). Effect of cerium oxide addition on the optical absorption edge of tungsten trioxide. *Journal of materials science*, 28(1), 239-242.
- [31] E. Broclawik, A. Góra, P. Liguzinski, P. Petelenz & M. Slawik (2005). Quantum chemical modelling of the process of lithium insertion into WO₃ films. *Catalysis today*, 101(2), 155-162.
- [32] S. R. Alharbi & A. F. Qasrawi (2018). Optical dynamics in the Ag/ α -Ga₂S₃ layer system. *Materials Science in Semiconductor Processing*, 83, 102-106.
- [33] S. K. Chong, C. F. Dee & S. A. Rahman (2015). Single reactor deposition of silicon/tungsten oxide core-shell heterostructure nanowires with controllable structure and optical properties. *RSC Advances*, 5(3), 2346-2353.
- [34] Kumar, Challa SSR, ed.(2015). *X-ray and Neutron Techniques for Nanomaterials Characterization*. Springer Berlin Heidelberg.
- [35] S. R. Alharbi & A. F. Qasrawi (2018). Gold and ytterbium interfacing effects on the properties of the CdSe/Yb/CdSe nanosandwiched structures. *Current Applied Physics*, 18(8), 946-951.
- [36] S. E. Al Garni, and A. F. Qasrawi. (2017) "Effect of Indium nano-sandwiching on the structural and optical performance of ZnSe films." *Results in physics* 7, 4168-4173.
- [37] A. Biot, Maurice(1965) *Mechanics of incremental deformations*.
- [38] A. K. Bhargava, and C. P. Sharma (2011). *Mechanical Behaviour and testing of materials*. PHI Learning Pvt. Ltd.

- [39] R. A. Levy, Ed. (2012). *Microelectronic materials and processes*, Springer Science & Business Media, 164
- [40] C. Kittel, and M.E. Pau. (1996) *Introduction to solid state physics*, New York: Wiley, 8.
- [41] M. Fox, (1970). Optical properties of solids.
- [42] Pankove, Jacques I. *Optical processes in semiconductors*. Courier Corporation, 2012.
- [43] D. Gust, T. A. Moore, & A. L. Moore, (2009). Solar fuels via artificial photosynthesis. *Accounts of chemical research*, 42(12), 1890-1898.
- [44] Dresselhaus, Mildred, Gene Dresselhaus, Stephen B. Cronin, and A. Gomes Souza Filho, (2018). *Solid State Properties*. Springer-Verlag Berlin Heidelberg.
- [45] Schrieffer, John Robert, (2007). *Handbook of high-temperature superconductivity: theory and experiment*. Edited by James S. Brooks.
- [46] E. H. Rhoderick, (1982). Metal-semiconductor contacts. *IEE Proceedings I-Solid-State and Electron Devices*, 129(1), 1.
- [47] S. M. Sze, & K. K. Ng, (2006). *Physics of semiconductor devices*. John wiley & sons.
- [48] W. Mönch, (2013). *Semiconductor surfaces and interfaces*. Springer Science & Business Media, (26).
- [49] S. Kar, (2013). *High permittivity gate dielectric materials*. Heidelberg: Springer, (43)
- [50] Sergey N. Makarov, Reinhold Ludwig, Stephen J. Bitar, (2016), Practical Electrical Engineering , 9-31.
- [51] S. E. Al Garni, and A. F. Qasrawi. (2017). "Impedance Spectroscopic Analysis of the InSe/ZnSe/InSe Interface." *IEEE Transactions on Electron Devices* 64.1, 244-249.
- [52] Darimireddy, Naresh Kumar, R. Ramana Reddy, and A. Mallikarjuna Prasad, (2015). "Design of triple-layer double U-slot patch antenna for wireless applications." *Journal of applied research and technology* 13.5 526-534.
- [53] B. M. Weckhuysen, J. M. Jehng & I. E. Wachs, (2000). In situ Raman spectroscopy of supported transition metal oxide catalysts: $^{18}\text{O}_2$ – $^{16}\text{O}_2$ Isotopic Labeling Studies. *The Journal of Physical Chemistry B*, 104(31), 7382-7387.

- [54] G. M. Ramans, J. V. Gabrusenoks, A. R. Lasis, & A. A. Patmalnieks, (1987). Structure of amorphous thin films of WO_3 and MoO_3 . *Journal of Non-Crystalline Solids*, 90(1-3), 637-640.
- [55] S. R. Alharbi & A. F. Qasrawi, (2017). Effect of ytterbium, gold and aluminum transparent metallic substrates on the performance of the Ga_2S_3 thin film devices. *Current Applied Physics*, 17(6), 835-841.
- [56] S. R. Alharbi, and A. F. Qasrawi, (2017) "Dielectric Dispersion in Ga_2S_3 Thin Films." *Plasmonics*, 12 (4) 1045-1049.
- [57] E. O. Nazzal, A. F. Qasrawi, & S. R. Alharbi, (2018). Engineering the Optical and Dielectric Properties of the $\text{Ga}_2\text{S}_3/\text{In}/\text{Ga}_2\text{S}_3$ Nanosandwiches via Indium Layer Thickness. *Plasmonics*, 13(3), 1049-1056.
- [58] S. R. Alharbi, & A. F. Qasrawi, (2019). Characterization of the $\text{Ge}/\text{Bi}_2\text{O}_3$ Interfaces. *Materials Research*, 22(3).
- [59] S. E. Al Garni, & A. F. Qasrawi, (2019). Fabrication and characterization of $\text{Yb}/\text{MoO}_3/(\text{C}, \text{Yb})$ devices. *Current Applied Physics*, 19(5), 639-645.
- [60] Z. F. Zhou, G. K. Ren, X. Tan, R. Liu, C. Liu, Y. H. Lin, & C. W. Nan, (2018). Enhancing the thermoelectric performance of ZnO epitaxial films by Ga doping and thermal tuning. *Journal of Materials Chemistry A*, 6(47), 24128-24135.
- [61] F. Gao, C. J. Wang, X. C. Liu & C. S. Tian, (2007). Effect of tungsten on the structure and piezoelectric properties of PZN–PZT ceramics. *Ceramics international*, 33(6), 1019-1023.
- [62] K. Xu, S. Tian, J. Zhu, Y. Yang, J. Shi, T. Yu, & C. Yuan, (2018). High selectivity of sulfur-doped SnO_2 in NO_2 detection at lower operating temperatures. *Nanoscale*, 10(44), 20761-20771.
- [63] Sharif, M. Kashif, M. A. Khan, M. F. Warsi, M. Ramzan, and A. Hussain, (2018). "Structural and ferroelectric properties of hafnium substituted BiFeO_3 multiferroics synthesized via auto combustion technique." *Ceramics International* 44(17), 20648-20655.
- [64] S. Sungping, C. g Shu, and L. Hwa, (1998). "Structure and properties of lanthanum galliogerminate glasses." *Journal of non-crystalline solids* 240, no. 1-3, 22-28.
- [65] L. Deng, G. Zhao, H. Zhong, S. Wang, & G. Liu, (2016). Investigation on the selectivity of N-((hydroxyamino)-alkyl) alkylamide surfactants for scheelite/calcite flotation separation. *Journal of Industrial and Engineering Chemistry*, 33, 131-141.

- [66] L. Ju, Y. Dai, W. Wei, M. Li, & B. Huang, (2018). DFT investigation on two-dimensional GeS/WS₂ van der Waals heterostructure for direct Z-scheme photocatalytic overall water splitting. *Applied Surface Science*, 434, 365-374.
- [67] M. T. Bedialauneta, E. Fernandez, I. Albizu, A. J. Mazon, & K. J. Sagastabeitia, (2013). Factors that affect the sag-tension model of an overhead conductor. In *2013 IEEE Grenoble Conference* (pp. 1-6). IEEE.
- [68] A. F. Qasrawi, (2018). Investigation of the structural and optoelectronic properties of the Se/Ga₂S₃ heterojunctions. *Journal of Alloys and Compounds*, 769, 78-82.
- [69] S. Keshri, A. Kumar & D. Kabiraj, (2011). Effect of Annealing on Structural, Optical and Electrical Behaviours of WO₃ Thin Films Prepared by Physical Vapour Deposition Method. *Journal of Nano-and Electronic Physics*, 3(1), 260.
- [70] R. Lin, J. Wan, Y. Xiong, K. Wu, W. C. Cheong, G. Zhou, ... & Y. Li, (2018). Quantitative study of charge carrier dynamics in well-defined WO₃ nanowires and nanosheets: insight into the crystal facet effect in photocatalysis. *Journal of the American Chemical Society*, 140(29), 9078-9082.
- [71] Y. Shimizu, N. Matsunaga, T. Hyodo, & M. Egashira, (2001). Improvement of SO₂ sensing properties of WO₃ by noble metal loading. *Sensors and Actuators B: Chemical*, 77(1-2), 35-40.
- [72] A. F. Qasrawi, & O. A. Omareya, (2018). Characterization of the Al/Ge/In₂Se₃/Ga₂S₃/Al hybrid tunneling barriers designed for Gigahertz/Terahertz applications. *Thin Solid Films*, 660, 276-281.
- [73] G. Halek, I. D. Baikie, H. Teterycz, P. Halek, P. Suchorska-Woźniak, & K. Wiśniewski, (2013). Work function analysis of gas sensitive WO₃ layers with Pt doping. *Sensors and Actuators B: Chemical*, 187, 379-385.
- [74] H. L. Skriver, & N. M. Rosengaard, (1992). Surface energy and work function of elemental metals. *Physical Review B*, 46(11), 7157.
- [75] Q. Niu, N. I. Crăciun, G. J. A. Wetzelaer, P. W. Blom, (2018). Physical review letters 120(11), 16602.
- [76] N. M. Khusayfan, A. F. Qasrawi, H. K. Khanfar, (2018). Materials Research Express 5(2), 026303.
- [77] S. E. Al Garni, & A. F. Qasrawi. (2018). Formation and negative capacitance effect in Au/Bi₂O₃/ZnS/Ag heterojunctions designed as microwave resonators. *Chalcogenide Letters*, 15(12).

[78] C. H. Wu, M. S. Feng, & C. C. Wu. (1993). Effect of Doping on the Growth of InGaP by Low Pressure Metalorganic Chemical Vapor Deposition. *MRS Online Proceedings Library Archive*, 300.

Appendix A

Starting with the expression of the absorption coefficient (α) in order to derive Tauc equation

$$\alpha = \frac{(\hbar\omega)(\text{transition probability / volume time})}{\text{total } I} \quad (\text{A.1})$$

$$\alpha = \frac{(\hbar\omega) w_{i \rightarrow f}}{I} \quad (\text{A.2})$$

Where ω is the angular frequency of photon, \hbar is Planck's constant $= h/2\pi = 1.054 \times 10^{-34}$ J.s and $w_{i \rightarrow f}$ is a quantum transition from a lower state to a higher state with a photon of angular frequency of ω , $w_{i \rightarrow f}$ was reported to take the form,

$$w_{i \rightarrow f} = \frac{2\pi}{\hbar} |M|^2 g(\hbar\omega) \quad (\text{A.3})$$

M is a matrix describes the perturbation of electron due to the light and $g(\hbar\omega)$ is the density of states.

$$M = \langle f | H' | i \rangle \quad (\text{A.4})$$

Or it can be written in the integral form as

$$M = \int \psi_f^*(r) H' \psi_i^*(r) d^3 r \quad (\text{A.5})$$

H' is the perturbation that is caused by light interaction with electrons, (i, f) are the initial and final states and r is the position of electron.

The external perturbation that couples initial and final states can be expressed by

$$H = \frac{e}{m_0} \vec{A} \cdot \vec{p} \quad (\text{A.6})$$

Where $\vec{p} = i\hbar\partial$ is the momentum of electron, \vec{A} is a vector potential of the incident field and m_0 is the mass of free electron.

Where \vec{A} can be expressed as

$$\vec{A}(r, t) = A_0 e^{i(kr - \omega t)} \quad (\text{A.7})$$

The exponential term can be understood by the Taylor series, $(\mathbf{k} \cdot \mathbf{r}) \sim 10^{-3}$, where $k \cdot r$ equals $\frac{2\pi r}{\lambda}$

Because of the wavelength at the optical frequency is $1.0 \mu\text{m}$ and the dimension of the atom size is nearly 10^{-10} m so that $(\mathbf{k} \cdot \mathbf{r}) \sim 10^{-3}$ which is very small so Taylor series can be used.

The presence of an electric field shifts the energy of charged particles of $-\rho E$, ρ is the electric dipole moment and E is the electric field of the light which given by

$$E(r)_{\text{photon}} = E_0 e^{ik \cdot r} \quad (\text{A.8})$$

$$\rho_e = -er \quad (\text{A.9})$$

Thus, the appropriate perturbation is

$$H' = -\rho_e \cdot E \quad (\text{A.10})$$

Substitute Eqn. (A.8) and (A.9) in (A.10) we obtain

$$H' = eE_0 e^{ik \cdot r} r \quad (\text{A.11})$$

Describing the electron wave function by Bloch theorem as

$$\psi_i(r) = \frac{1}{\sqrt{V}} u_i(r) e^{ik \cdot r} \quad (\text{A.12})$$

$$\psi_f(r) = \frac{1}{\sqrt{V}} u_f(r) e^{ik \cdot r} \quad (\text{A.13})$$

Where V is the normalization volume, $u_i(r)$, $u_f(r)$ are appropriate periodic functions and k_i , k_f are the wave vector of the initial and final states of the electron, so M becomes

$$M = \frac{e}{V} \int u_f^*(r) e^{-ik_f \cdot r} E_o r e^{ik_i \cdot r} u_i^*(r) e^{ik_i \cdot r} d^3 r \quad (\text{A.14})$$

Two consideration must be taking into consideration to solve this integral, first is the conservation of the momentum (photon momentum must equal the change in the electron momentum) and the second is that Bloch's theorem requires that both $u_i(r)$ and $u_f(r)$ are periodic functions.

The density of electron states in the band per unit energy is $g(\hbar\omega)$

$$g(E) dE = 2 g(k) dk \quad (\text{A.15})$$

$g(k)$ is the density of state in momentum space. The number 2 in the equation is related to the presence of electron spin state.

$$g(E) = \frac{2g(k)}{dE/dk} \quad (\text{A.16})$$

dE/dk is the gradient of E-k curve in the band diagram, $g(k)$ is the number of state per unit volume in k-space, that mean $1/(2\pi)^3$ is multiplied by incremental volume from k to $k + dk$ which is $4\pi k^2 dk$, thus $g(k)$ becomes

$$g(k) dk = \frac{k^2}{2\pi^2} dk \quad (\text{A.17})$$

$$g(k) = \frac{k^2}{2\pi^2} \quad (\text{A.18})$$

Eqn. (A.16) becomes

$$g(E) = \frac{1}{2\pi^2} \left(\frac{2m^*}{\hbar^2} \right)^{3/2} E^{1/2} \quad (\text{A.19})$$

Where m^* is known as the mass effective.

Using the conservation of energy which state that

$$\hbar\omega = E_g + \frac{\hbar^2 k^2}{2m_c^*} + \frac{\hbar^2 k^2}{2m_{hole}^*} \quad (A.20)$$

E_g is the energy band gap

The reduced mass can be defined as

$$\frac{1}{\mu} = \frac{1}{m_c^*} + \frac{1}{m_{hole}^*} \quad (A.21)$$

Substitute Eqn. (A.21) in Eqn. (A.20) we have

$$\hbar\omega = E_g + \frac{\hbar^2 k^2}{2\mu} \quad (A.22)$$

$$g(\hbar\omega) = \begin{cases} \frac{1}{2\pi^2} \left(\frac{2\mu}{\hbar^2}\right)^{3/2} (\hbar\omega - E_g)^{1/2}, & \text{when } \hbar\omega > E_g \\ 0, & \text{when } \hbar\omega < E_g \end{cases} \quad (A.23)$$

Using Eqns. (A.3) and (A.23) to simplify Eqn. (A.2), we get

$$\alpha = c \frac{(\hbar\omega - E_g)^{1/2}}{\hbar\omega} \quad (A.24)$$

Where c is a constant

$$\alpha\hbar\omega = c(\hbar\omega - E_g)^{1/2} \quad (A.25)$$

$$\alpha\hbar\omega \propto (\hbar\omega - E_g)^{1/2} \quad (A.26)$$

Eqn. (A.25) represent Tauc equation of direct allowed band gap ($p = 1/2$). In general,

Tauc relation states that,

$$\alpha\hbar\omega \propto (\hbar\omega - E_g)^p \quad (A.27)$$

Where $\hbar\omega$ is the photon energy, from plotting $(\alpha E)^{1/p}$ versus E , and taking the widest linear region using linear fitting, the energy gap for semiconductor can be determined from the intercept of the E-axis.

Appendix B

Suppose an electric field in the x-axis and propagating in the z direction include both of the reflected and incident waves.

$$\vec{E}_x = E_0 e^{i(kz - \omega t)} \quad (\text{B.1})$$

Where k is the wave vector and ω is the angular frequency. E_0 is the amplitude at $z = 0$.

k and ω are therefore related to each other through:

$$k = \frac{2\pi}{(\lambda/n)} = \frac{n\omega}{c} \quad (\text{B.2})$$

That can be generalized and using complex refractive index:

$$k = \frac{\omega}{c} \tilde{N}_{complex} \quad (\text{B.3})$$

$$\vec{E}_x = E_0 e^{i(\omega \tilde{N}/c - \omega t)} \quad (\text{B.4})$$

$$= E_1 e^{i(\frac{\omega z}{c} - \omega t)} + E_2 e^{-i(\frac{\omega z}{c} + \omega t)} \quad (\text{B.5})$$

$$E_o = E_1 + E_2 \quad (\text{B.6})$$

Where E_o , E_1 and E_2 are relating by the continuity equation for the tangential component of H_y across the boundary of the solid, using Maxwell's equation

$$\nabla \times \vec{E} = -\frac{\mu}{c} \frac{\partial \vec{H}}{\partial t} = \frac{i\omega\mu}{c} \frac{\partial \vec{H}}{\partial t} \quad (\text{B.7})$$

$$\frac{\partial \vec{E}_x}{\partial z} = \frac{i\omega\mu}{c} \frac{\partial \vec{H}}{\partial t} \quad (\text{B.8})$$

Derive Eqn. (B.5) we get

$$E_o k = E_1 \frac{\omega}{c} - E_2 \frac{\omega}{c} = E_o \frac{\omega}{c} \tilde{N}_{complex} \quad (\text{B.9})$$

$$E_1 - E_2 = E_o \tilde{N}_{complex} \quad (\text{B.10})$$

Solving the equations (B.10) and (B.6) we get

$$E_2 = \frac{1}{2} E_o (1 - \tilde{N}_{complex}) \quad (B.11)$$

$$E_1 = \frac{1}{2} E_o (1 + \tilde{N}_{complex}) \quad (B.12)$$

The normal incident reflectivity is given by the relation,

$$R = \left| \frac{E_2}{E_1} \right|^2 \quad (B.13)$$

Simplifying Eqn. (B.13) by substituting equations (B.11) and (B.12)

$$R = \left| \frac{(1 - \tilde{N}_{complex})}{(1 + \tilde{N}_{complex})} \right|^2 \quad (B.14)$$

Where $\tilde{N}_{complex}$ consists of real and imaginary parts, $\tilde{N}_{complex} = n + iK$

$$R = \frac{1 + n^2 - 2n + K^2}{1 + n^2 + 2n + K^2} \quad (B.15)$$

Suppose that $n = K \gg 1$ (strongly absorbing medium, larger value of n and K) [41], so the unity terms are cancelled, Eqn. (B.15) becomes

$$Rn^2 + 2nR + K^2R = n^2 - 2n + K^2 \quad (B.16)$$

$$(R-1)n^2 + 2n(R+1) + K^2(R-1) = 0 \quad (B.17)$$

using the solution of square root equation

$$x = \frac{-b \pm \sqrt{b^2 - 4ac}}{2a} \quad (B.18)$$

we obtain

$$n = \frac{-2(R+1) \pm \sqrt{(2(R+1))^2 - (4(R-1)(R-1)K^2)}}{2(R-1)} \quad (B.19)$$

$$n = - \left(\frac{R+1}{R-1} \right) \pm \sqrt{\left(\frac{R+1}{R-1} \right)^2 - K^2} \quad (B.20)$$

The roots are

$$n_1 = -\left(\frac{R+1}{R-1}\right) + \sqrt{\left(\frac{R+1}{R-1}\right)^2 - K^2}$$

$$n_2 = -\left(\frac{R+1}{R-1}\right) - \sqrt{\left(\frac{R+1}{R-1}\right)^2 - K^2}$$

We know that

$$n = \sqrt{\mathcal{E}_{eff}} \quad (B.21)$$

Substitute Eqn. (B.21) in equation (B.20) we get

$$\sqrt{\mathcal{E}_{eff}} = -\left(\frac{R+1}{R-1}\right) - \sqrt{\left(\frac{R+1}{R-1}\right)^2 - K^2} \quad (B.22)$$

It is important to define the complex refractive index to derive the dielectric constant formulas have to introduced

$$\tilde{N}_{complex} = \sqrt{\mu\mathcal{E}} \quad (B.23)$$

Where $\tilde{N}_{complex}$ consists of real and imaginary parts

$$\tilde{N}_{complex} = n + iK \quad (B.24)$$

$$K = \frac{\omega}{c} \tilde{N}_{complex} \quad (B.25)$$

Equation (B.21) can be derived from Maxwell's equations, n is the refractive index and K is the extinction coefficient.

For non-magnetic material ($\mu=1$) then Eqn.(B.23) becomes

$$\tilde{N}_{complex} = \sqrt{\mathcal{E}_{eff}} \quad (B.26)$$

The dielectric constant formula is given by,

$$\mathcal{E}_{eff} = \mathcal{E}_r + i\mathcal{E}_{im} \quad (B.27)$$

\mathcal{E}_r and \mathcal{E}_{im} represents the real and imaginary parts of dielectric, respectively.

Substitute Eqn. (B.26) in Eqn. (B.24) we get,

$$\tilde{N}_{complex}^2 = \varepsilon_{eff} = (n + iK)^2 \quad (B.28)$$

$$\varepsilon_{eff} = n^2 - K^2 + i2nK \quad (B.29)$$

Comparing Eqn. (B.27) with Eqn. (B.29) the real and imaginary parts are

$$\varepsilon_r = n^2 - K^2 \quad (B.30)$$

$$\varepsilon_{im} = 2nK \quad (B.31)$$

To find the relation between K and α consider that an electromagnetic wave propagate in a medium in the z -direction with an electric field of

$$E(z, t) = E_o e^{i(kz - \omega t)} \quad (B.32)$$

Where k is the wave number and ω is the angular frequency, the relation between the extinction coefficient K and λ is

$$K = \frac{2\pi}{\lambda/N} \quad (B.33)$$

Combining Eqns. (B.24), (B.25), (B.32) and (B.33)

$$K = \frac{\omega}{c} (n + iK) \quad (B.34)$$

$$E(z, t) = E_o e^{i(\frac{\omega n z}{c} - \omega t)} e^{-\frac{k z \omega}{c}} \quad (B.35)$$

We know that the optical intensity of light wave is proportional to the square of the electric field where $I \propto EE^*$

$$I \propto e^{\left(\frac{-k\omega z}{c}\right)} \quad (B.36)$$

If equation (B.36) is compared with Beer' equation (2.10) we can find that

$$2 \frac{K\omega}{c} = \alpha = \frac{4\pi K}{\lambda} \quad (B.37)$$

Then,

$$K = \frac{\lambda\alpha}{4\pi} \tag{B.38}$$

الملخص

في هذه الأطروحة، قمنا بتصميم وتشخيص رقائق أكسيد التنغستون/كبريتات الغاليوم المهجنة المتغايرة الموصلية وغير المتجانسة. تم دراسة التركيبة المتغايرة والمصنعة باستخدام تقنية التبخير الحراري تحت ضغط الفراغ 10^{-5} ملبار عن طريق حيود الأشعة السينية، المسح المجهر الإلكتروني، مطيافية الأشعة السينية المشتتة للطاقة، محلل الطيف المرئي والفوق بنفسجي، مطياف المقاومة وخصائص منحنيات المواسعة والتيار تحت تأثير الجهد. بينما أشار حيود الأشعة السينية إلى وجود طبيعة غير متبلورة للمواد المصنعة، فإن صور الماسح الإلكتروني لم تعرض أي شكل معين مؤكدا الطبيعة غير المتبلورة للرقائق النامية. ويعرض تحليل مطياف الأشعة السينية المشتتة عدم وجود شوائب بداخل المواد. بصريًا، بينما تبين أن قيم فجوات الطاقة لأكسيد التنغستون وكبريتات الغاليوم هي 3.17 و 2.53 إلكترون.فولت، على التوالي. فإن واجهة أكسيد التنغستون/كبريتات الغاليوم تظهر فجوة طاقة قدرها 2.62 إلكترون.فولت ويؤدي هذا إلى عدم وجود انقطاع في مستويات طاقة التوصيل وانفصال في مستويات طاقة التكافؤ بقيمة 0.61 إلكترون.فولت وتظهر الطبقات البينية بصريًا ذيلًا عميق النطاق بعرض 0.78 إلكترون.فولت. بالإضافة إلى ذلك، أظهرت القياسات الكهربائية أن تحضير الطبقات المتغايرة على رقائق الايتريوم ثم تبخير مخدات توصيل من رقائق الذهب على هذه الطبقات يجعل التركيبة الفيزيائية صالحة للاستخدام كجهاز MOSFET كما تشير منحنيات السعة - الجهد. وبينت منحنيات الجهد والتيار أيضًا ميزات الترشيح الكهربائي مما يجعله مناسبًا لتصام ثنائي. من ناحية أخرى، أوضح التحليل الطيفي للمقاومة أن التركيبة الفيزيائية المتغايرة يمكنها إظهار قدرة كبيرة على معايرة المواسعة والمقاومة في مجال التردد من 10-1800 ميغاهرتز. ولوحظ أيضًا أن الأجهزة المهجنة $Yb / WO_3 / Ga_2S_3 / Au$ لديها القدرة على العمل كمرشحات للأمواج الميكروية ومرشحات موقفة للأمواج عند تردد قدره 1.65 جيغاهرتز. أظهر اختبار قيم ضياع طاقة الموجة بين الموجات المتناوبة أن الإشارة بين الإرسال والاستقبال ذات جودة عالية مما يجعل مرشحات الموجة الميكروية واعدة.

